

1 **Tracing future spring and summer drying in southern Africa to**
2 **tropical lows and the Congo Air Boundary**

3 Emma Howard* and Richard Washington

4 *School of Geography and the Environment, University of Oxford, Oxford, United Kingdom*

5 * *Corresponding author*: Emma Howard, emma.howard@reading.ac.uk

ABSTRACT

6 In southern Africa, models from the 5th Coupled Model Intercomparison Project (CMIP5)
7 predict robust future drying associated with a delayed rainy season onset in the Austral
8 spring and a range of wetting and drying patterns in the Austral summer. This paper
9 relates these rainfall changes to dynamical shifts in two classes of weather systems: the
10 Congo Air Boundary (CAB) and tropical lows. Objective algorithms are used to track these
11 features in CMIP5 model output. It is then established that the climatological locations and
12 frequencies of these systems are reasonably well represented in the CMIP5 models. RCP8.5
13 end of 21st century projections are compared with historical end of 20th century simulations.
14 Future projections in tropical low locations and frequencies diverge, but indicate an overall
15 average decrease of 15% and in some cases a northward shift. The projected spatial change
16 in the tropical low frequency distribution is weakly positively correlated to the projected
17 spatial change in the Austral summer rainfall distribution. Meanwhile, future projections
18 indicate a 13% increase in CAB frequency from October to December. This is associated
19 with the gradual climatological CAB breakdown occurring half a month later on average in
20 end of 21st century RCP8.5 projections. A delay in the gradual seasonal decline of the CAB
21 prevents rainfall to the south of the CAB's mean position, most of which is shown to occur
22 on CAB breakdown days, hence creating the Austral spring drying signal and delayed wet
23 season onset. Inter-model variability in the magnitude of CAB frequency increase is able to
24 explain inter-model variability in the projected drying.

25 1. Introduction

26 CMIP5 based rainfall projections exhibit a rainfall decline over southern Africa which is
27 strongest in the October, November and December (OND) season (James and Washington
28 2013). This rainfall decline has been linked with a delay in the onset date of the rainy
29 season (Dunning et al. 2018), and in many models comes with an increase in rainfall in
30 central Africa in the same season (Aloysius et al. 2016; Creese et al. 2019). Southern Africa
31 is highly vulnerable to climate related socio-economic risk, as the regional water resource
32 supports the local food-energy-water nexus (Conway et al. 2015). In particular, rainy season
33 onset and cessation dates are particularly important for farmers and other stakeholders
34 (Hachigonta et al. 2008). Some studies have found consistent delays of southern African
35 wet season onset in satellite and gauge-based observational datasets covering the late 20th
36 and early 21st centuries (e.g., Jiang et al. 2019; Kniveton et al. 2009). Delayed rainfall
37 onset would shorten the growing season, as no corresponding delay in cessation has been
38 projected (Dunning et al. 2018). This will reduce the agricultural viability of the region and
39 have follow-on effects on regional food security and economic growth (Lobell et al. 2008;
40 Schlenker and Lobell 2010).

41 At first glance, the southern African drying trend appears to follow that of the broader
42 subtropical drying trend. However, closer analysis reveals that in southern Africa, the drying
43 occurs primarily north of the subtropical rainfall minimum (Scheff and Frierson 2012a,b).
44 Furthermore, while the subtropical drying signal is largely characterized by an increase in the
45 magnitude of the difference between precipitation and evaporation (P-E), in southern Africa
46 evaporation decreases in line with precipitation, so that P-E does not change considerably.
47 Lazenby et al. (2018) demonstrated that the southern African drying trend is primarily a

48 consequence of circulation changes, rather than thermodynamic mechanisms such as dry-
49 get-drier (Held and Soden 2006) or upped-ante (Chou et al. 2009). Thus, the southern
50 African drying trend is dynamically unique and requires a bespoke approach.

51 Some work has been done on understanding the dynamics of projected rainfall change in
52 southern Africa. Lazenby et al. (2018) found that this change could be viewed as a northward
53 shift of the African rain-band, while Dunning et al. (2018) linked the delayed onset of OND
54 rains in southern Africa to relative changes in the strengths of the Saharan and Angolan
55 heat lows. Munday and Washington (2019) found a complementary result: models with a
56 deeper future climatological Angola heat low showed a higher intensity of drying. Similarly,
57 Cook and Vizzy (2013) observed a strengthening of the Angola low in regional climate model
58 simulations. However, little work has been done to directly link rainfall change to changes
59 in precipitating weather systems.

60 Meanwhile, less work has looked at rainfall change in December - February (DJF), the
61 peak of the wet season (Van Heerden and Taljaard 1998). Model projections disagree in this
62 season, although Lazenby et al. (2018) suggest that inter-model differences in SST trends
63 in adjacent oceans may explain the diverse range of model projections. Once again, the
64 characteristics of the future change patterns of atmospheric features on synoptic timescales
65 has not been studied.

66 Since atmospheric circulation on climatological timescales is the aggregation of synoptic
67 weather systems, future circulation change hinges on the response of synoptic weather sys-
68 tems to a warmer atmosphere. However, the synoptic weather systems that occur in the
69 southern African tropical margins are under-studied. The representation of such synoptic
70 weather systems in CMIP5 models and their future change has not been studied. This
71 knowledge gap ensures that the synoptic context of the future change signal in this region,

72 and whether or not a specific class of weather system may deliver the projected change, is
73 unknown.

74 This paper focusses on two local classes of weather systems which occur in the latitudi-
75 nal band of the advancing spring rains and have previously been associated with rainfall
76 variability. The first is the Congo Air Boundary (CAB), a combined surface dryline and
77 convergence line that marks the boundary between tropical and subtropical weather zones
78 in the Austral spring (Howard and Washington 2019). The second class of weather systems
79 considered are tropical lows, cyclonic rotating vortices that form in the Austral summer
80 and tend to cluster near 20°S, creating the climatological Angola tropical low (Howard and
81 Washington 2018). By examining the representation of the CAB and tropical lows in histor-
82 ical coupled climate models, this work follows a process based model evaluation framework.
83 After establishing whether these systems are well modelled, we then proceed to studying
84 process based projections. This involves investigating how the CAB and tropical lows are
85 projected to change according to RCP8.5 end of 21st century simulations.

86 Both of these weather systems were identified by Taljaard (1986) as two of the ten most
87 important factors that influence the weather over southern Africa. Crucially, they both
88 operate on length-scales that are large enough to be resolved in CMIP5 models. The focus
89 of this work is on the Austral spring and summer seasons, since the former is the season with
90 the strongest rainfall change, and the latter is the main rainy season. Our analysis will show
91 that changes in tropical lows and the CAB are vitally important for future projections of
92 southern African precipitation, as they directly influence the delivery of model precipitation.
93 However, this result does not preclude changes in other factors, including the distribution of
94 sea surface temperatures, the subtropical jet and high-pressure belt, and upper-level waves,

95 from also playing a role. Indeed, it is possible that the circulation changes of tropical lows
96 and the CAB are linked to changes in these other systems.

97 The CAB has historically been defined as the confluence zone between the Congo Airmass,
98 a moist and convectively active region of air that sits over the Congo rainforest, and the drier
99 trade easterlies that cross southern Africa and originate from the Indian Ocean (Taljaard
100 1972). The CAB was originally discussed in the context of identifying the elusive ITCZ
101 over southern and eastern Africa (Taljaard 1953). It was argued that the CAB could not
102 be the ITCZ itself, as both airmasses involved originate from the Southern Hemisphere (the
103 Congo Airmass being associated with the recurvature of the south Atlantic trade winds,
104 known locally as the low level westerlies, e.g., Leroux (2001)). However, the importance of
105 the CAB for southern African rainfall was undisputed (Torrance 1979).

106 Despite its importance to the local climate, no systematic study of the representation of the
107 CAB in reanalysis or model products had been performed before Howard and Washington
108 (2019). They optimized an edge-detecting algorithm and a ridge-detecting algorithm to
109 pick out sharp gradients in specific humidity and ridges in wind convergence that were
110 associated with the southern portion of the CAB. They distinguished between the ‘dryline’
111 CAB and a ‘convergence line’ CAB based on the choice of algorithm and determined that
112 although the two were closely comparable, the ‘dryline’ algorithm was slightly more reliable.
113 Howard and Washington (2019) also identified the Kalahari Discontinuity (KD), a similar
114 near-surface dryline/convergence line system located further south and oriented parallel to
115 the west coast of southern Africa, that forms after the CAB breaks down in October and
116 November. They confirmed that the CAB latitude and detection frequency were closely
117 linked to the interannual variability of spring rainfall over southern Africa. This suggests
118 that the future change of the CAB has potential explanatory power for the OND drying.

119 Southern African tropical lows are synoptic-scale cyclonic vortices with depths up to 500
120 hPa that track predominantly westward across the southern African continent (Howard and
121 Washington 2018). They are precipitating systems, and cluster in eastern Angola and west-
122 ern Zambia, where they tend to become semi-stationary (Howard et al. 2019). In southern
123 Africa, tropical lows have been most commonly studied in the form of their climatological
124 mean, the Angola tropical low (e.g., Cook et al. 2004; Cr  tat et al. 2018; Pascale et al.
125 2019). Since the Angola tropical low has been closely linked to interannual rainfall variabil-
126 ity (Reason and Jagadheesha 2005; Cook et al. 2004), considerable attention has been paid
127 to how it is simulated in various models. Lazenby et al. (2016) and Munday and Washington
128 (2017) both found that the Angola low is excessively strong in historical climate models,
129 and linked this to the wet bias over southern Africa. However, the representation of the
130 Angola tropical low on synoptic timescales in CMIP5 models, and its future change, has not
131 yet been assessed.

132 The goal of this paper is to express projected rainfall changes from the viewpoint of
133 projected changes in synoptic weather systems. This involves first linking the spring drying
134 signal to projected changes in characteristics of the CAB, and also linking the summer inter-
135 model spread of rainfall projections with the inter-model spread of changes to the spatial
136 distribution and frequencies of tropical lows and the CAB. To achieve this aim, the paper
137 proceeds as follows. In section 2, the models, datasets and feature identification algorithms
138 are described. In section 3, we consider the historical representation of the CAB, the CAB’s
139 projected future change and the rainfall implications of that projected change. In section
140 4, we perform a similar analysis on tropical lows. In the final section, we summarize the
141 importance of this work for understanding rainfall change in southern Africa.

142 2. Methods

143 *a. Models and Reanalysis Datasets*

144 A selection of 25 CMIP5 models has been used in this study, based on the availability of
145 the appropriate model output variables. To study the CAB, we require daily surface level
146 specific humidity and temperature data, which 18 of these models had available. To study
147 tropical lows, we required 6 hourly wind data on pressure levels, which was available in
148 a different subset of 18 models. The model names, creators and grid-spacings are shown
149 in table 1, together with a list of which models were used to study the CAB and tropical
150 lows. For each model, 30 years of end of 20th century coupled climate model output were
151 examined, and compared to 30 years of end of 21st century model output generated under
152 the RCP8.5 coupled model scenario. More precisely, the CAB was studied between August
153 '70 and December '99 of each century, while tropical lows were studied between November
154 '69 and March '99. The simulated historical climatology of each feature was compared
155 to the reanalysis climatologies from three reanalysis products: ERA-5, ERA-Interim and
156 MERRA-2. Reanalysis climatologies were taken from the 30-year period 1980-2010.

157 The CAB has been identified between August and December, and its correlation with
158 rainfall change has been studied between October and December. The former season has
159 been chosen because this is the season in which the CAB is present in southern Africa, and
160 the season in which validation against the results of Howard and Washington (2019) was
161 possible. The latter season was chosen because it is the season of maximum rainfall decline
162 in southern Africa (Munday and Washington 2019). Tropical lows were identified between
163 November and March, and their influence on future rainfall change was studied between
164 December and February. Again, the former is the season in which tropical lows are present

165 in southern Africa (Howard et al. 2019). The latter is the main wet season in southern
166 Africa, and is also the season in which the contribution of tropical lows towards southern
167 African rainfall is most significant (Howard et al. 2019). The OND precipitation decline
168 across the two 30-year time periods is greater than the 30-year decadal standard deviation
169 as calculated from the corresponding pre-industrial control experiments in over 50% of the
170 models considered, as indicated by Supplementary Figure S1. This was not the case in DJF.

171 *b. Congo Air Boundary*

172 This paper adapts the methodology of Howard and Washington (2019) to identify the
173 CAB in CMIP5 models. Because they studied the CAB in a high resolution ($\sim 0.25^\circ$)
174 reanalysis dataset, and the models employed here have resolutions ranging from $\sim 1^\circ - 3^\circ$,
175 this methodology needs a few modifications in order to transfer over to lower resolutions.
176 Properties of the CAB are dependent on the resolution of the input data, and so all models
177 and reanalyses are regridded to a $2^\circ \times 2^\circ$ grid.

178 While Howard and Washington (2019) used both wind convergence and humidity to detect
179 the CAB, the present study only uses humidity, and focusses solely on what Howard and
180 Washington (2019) refer to as the ‘dryline CAB’. This choice was made because Howard and
181 Washington (2019) found that the dryline CAB was more reliable and easily detected than
182 the convergence line CAB. Near-surface relative humidity gradients, rather than specific
183 humidity gradients, have been used to calculate the CAB location. This choice has been
184 made to allow for easier comparison between historical and RCP8.5 experiments, given that
185 near-surface specific humidity generally increases by a factor of about two across the tropics
186 by the end of the 21st century in the RCP8.5 scenario.

187 The algorithm used to detect the CAB is as follows. Figure 1 shows the algorithm applied
188 to a sample day (9/9/1999) from a sample model (ACCESS1.3).

189 1. The 2m relative humidity is calculated from 2m daily mean air temperature (*tas*), 2m
190 daily mean specific humidity (*huss*) and surface pressure (*sp*), where these fields are
191 available. Where they are not available, the 1000 hPa pressure level relative humidity
192 (*hur*) is used instead.

193 2. Relative humidity is interpolated to a $2^\circ \times 2^\circ$ grid using a nearest neighbor interpolation
194 scheme. This scheme is chosen in order to avoid differentially smoothing humidity
195 gradients in the higher resolution datasets during the regridding process. The left panel
196 of Figure 1 shows the regridded field.

197 3. In keeping with the Canny (Canny 1986) algorithm, a Gaussian filter with a 2° radius
198 is used to smooth the relative humidity field. The magnitude (M) and direction (θ) of
199 the gradient were then calculated using finite differences.

200 4. Canny edges were calculated as per Howard and Washington (2019), thresholding the
201 magnitude of the humidity gradient such that it must undergo an absolute change of
202 $\Delta RH = 40\%$ between grid cells across a Canny edge in order for a grid cell to qualify
203 as a CAB. The center panel of Figure 1 shows the Canny edges identified on the sample
204 model day, colored by the orientation angle of the edge.

205 5. Canny edges were filtered to retain instances with $-\frac{\pi}{4} < \theta < \frac{\pi}{6}$ and restricted to
206 latitudes between $5^\circ - 18^\circ\text{S}$.

207 6. At least 3 qualifying dryline grid cells were required to be detected at the same time
208 in order for a CAB to be registered. The resultant CAB grid-cells shown in the right
209 panel of Figure 1 on the sample model day.

210 The KD is also extracted from the calculated set of Canny edges. It is restricted to
211 latitudes below 12°S and angles between $\frac{\pi}{6} < \theta < \frac{\pi}{2}$, consistent with Howard and Washington
212 (2019). No minimum grid cell thresholds are applied in this case. As described above, three
213 reanalysis products, ERA-5, ERA-Interim and MERRA2, have been included in this study.
214 The thresholds described above were manually optimized so that the seasonal cycle of the
215 relative humidity based CAB in the coarsened ERA-5 using the methodology of this paper
216 was qualitatively similar to the high resolution specific humidity ERA-5 results of Howard
217 and Washington (2019).

218 Figure 2 shows the near-surface relative humidity and identified CAB points for the same
219 case study day in early September in historical models and reanalyses. The atmospheric
220 states on this chosen day will be in different synoptic setups. Nevertheless, a well-defined
221 CAB is identified on this day in all of the CMIP5 models.

222 With the daily CAB positions calculated, climatologies of properties such as latitude,
223 frequencies and extent can be computed and compared. Here, the extent is calculated by
224 counting the total number of CAB grid cells on a given day. This gives an approximate
225 measure of the lateral extent of the CAB.

226 *c. Tropical lows*

227 The methodology used to identify tropical low events follows Howard et al. (2019). We
228 apply the TRACK algorithm (Hodges 1994, 1999). The application of TRACK to CMIP5
229 model experiments has previously been documented by Rastogi et al. (2018) and Bengtsson

230 et al. (2007). Howard et al. (2019) identified southern African tropical lows using 6-hourly
231 vertical mean vorticity averaged across pressure levels at 600, 700 and 800 hPa. However,
232 6-hourly CMIP5 pressure level model data was only available at 850 and 500 hPa, and so
233 these model levels have been used instead. A comparison between the results of using this
234 set-up and using 600, 700 and 800 hPa daily vorticity was considered for a subset of 9 models
235 and no significant difference was found (not shown).

236 The data preparation algorithm was as follows. At each vertical level and for each 6-hourly
237 time-step, vertical vorticity was calculated from the zonal and meridional wind components
238 at a T63 resolution, using the python package windspharm. The vertical average was taken,
239 and then a Sardeshmukh and Hoskins (1988) filter was applied to smooth the spectral cut-
240 off. Cyclonic vorticity extrema with $\zeta < -5 \times 10^{-6} s^{-1}$ were then identified and linked using
241 the TRACK algorithm, as detailed in Howard et al. (2019) and Hodges et al. (2017). Once
242 these vortex tracks were identified, they were filtered for southern African tropical lows using
243 the following criteria:

- 244 1. Tracks must spend at least one time step over land;
- 245 2. Track longevity must be at least one day;
- 246 3. The filtered vertical mean relative vorticity must satisfy $\zeta < -3 \times 10^{-5} s^{-1}$ in at least
247 one 6-hourly time-step;
- 248 4. There must be coincident cyclonic vorticity at 500, 850 hPa for a continuous 24 hour
249 period;
- 250 5. The genesis location must not be in the Atlantic; and
- 251 6. The genesis location must be north of 25° S.

252 Justification for these criteria are given in Howard et al. (2019): briefly, they exclude extra-
253 tropical cyclones, coastally trapped Kelvin waves, heat lows, and spurious weak events. A
254 sample track longitude Hovmöller plot for each of the models and the reanalysis over one
255 historical year is shown in Figure 3. The models reveal a mixture of track behaviours.

256 Following the identification of tropical lows, rainfall is attributed to tropical lows by making
257 the assumption that all daily rainfall that fell within a 5° radius of a tropical low centroid
258 was attributable to that tropical low. This radius was shown to be appropriate for southern
259 African tropical lows by Howard et al. (2019) and is consistent with many previous studies
260 of tropical lows and tropical cyclones (Baray et al. 2003; Dare et al. 2012; Khouakhi et al.
261 2017; Lavender and Abbs 2013).

262 **3. The Congo Air Boundary**

263 *a. Representation in Historical Climate Models*

264 The aim of this section is to determine whether or not the CAB is well represented in the
265 CMIP5 historical simulations under consideration for the period from 1970-2000. Figures are
266 designed to be comparable with the ERA-5 based study of the CAB presented in Howard
267 and Washington (2019), and modelled CAB properties are compared with the coarsened
268 ERA-5 reanalysis. The KD is also briefly considered.

269 Figure 4 indicates the climatological location of the CAB and KD in each climate model
270 and reanalysis product, based on the frequency the CAB is detected at each interpolated
271 $2^\circ \times 2^\circ$ grid-box. It is evident that the CAB is detected with similar frequencies and locations
272 in most of the models as in the reanalysis products. There is a range of variation across the
273 models, however. CMRM-CM5, GFDL-CM3 and the ACCESS models show concentrated,

274 high intensity CAB locations with a diagonal orientation from west of Lake Victoria through
275 to south west Angola. NorESM1-M and bcc-csm1-1m show heat-maps with a distinct north
276 and south peak. All three IPSL models show low CAB detection frequencies in the east.
277 This is particularly interesting since the IPSL-CM5A models have previously been shown to
278 be outliers in East Africa, lacking the moisture-rainfall relationship present in most other
279 models (Rowell and Chadwick 2018). CanESM2 exhibits lower frequency CAB detection
280 rates than the other models, suggesting that it may struggle to represent the feature. The
281 biases of the spatial distribution of the CAB in these climate models relative to ERA-5
282 reanalysis, and their significance relative to natural variability over the 30-year time period,
283 are shown in Supplementary Figure S2. Overall, climate models exhibit biases that are
284 larger than the variability across the reanalysis products. However, the reanalysis products
285 do display some differences, particularly in the locations of peak CAB detection.

286 There is much more variability in the representation of the KD in CMIP5 models. BNU-
287 ESM shows a very persistent KD, while CSIRO-Mk3.6 and GFDL models represent it rea-
288 sonably well and some other models, such as CNRM-CM5 and CanESM2 miss it completely.
289 Meanwhile, MERRA-2 shows a more infrequent KD than the other reanalysis products. We
290 conclude that the KD is not as well represented in CMIP5 models as the CAB, and postpone
291 further analysis for a future study.

292 We next study the seasonal cycle of key CAB features in the CMIP5 models. The seasonal
293 cycles of the CAB latitude, frequency and extent in CMIP5 models and low resolution
294 reanalysis products are shown in Figure 5. The CAB latitude and extent are both calendar
295 day climatological means between 1970 and 2000, and all variables have been smoothed by
296 a 2-week running mean. The extent is calculated by counting the total number of CAB grid
297 cells on a given climatological day of the year. Only the days when a CAB was identified

298 were used in the average. This gives an approximate measure of the lateral extent of the
299 CAB, though it is not precisely comparable across CABs of different orientations. The
300 latitude shown is the mean latitude of all CAB points on a given day, and the frequency is
301 the proportion of days at a given time of year where a CAB is present.

302 Howard and Washington (2019) found that based on ERA-5 reanalysis, the CAB moves
303 steadily southward between the start of August and the end of November, and that its
304 detection frequency drops from near 100% at the start of October through to 10-20% at
305 the beginning of December. In the present study, similar behavior is present in the latitude
306 and frequency (the top and center panels respectively of Figure 5). The rate at which the
307 CAB moves south is close to constant across models and consistent with ERA-5, at roughly
308 2 degrees per month. Results from ERA-5 are located at the southern edge of the CMIP5
309 simulated range. At any given time of the year, the climatological CAB latitude has a
310 range of 5° . Since this range is of a similar order of magnitude to the Nyquist frequency
311 ($2\Delta x = 4^\circ$), we surmise that the CAB latitude is represented in these models as well as can
312 be expected. Based on the center panel of Figure 5, it is evident most models, as well as
313 the MERRA-2 reanalysis, show a decreased CAB frequency in August, however all models
314 except CAN-ESM2 recover by early September and the vast majority possess CABs that
315 are present 80% of the time. The CAB breaks down between October and December in all
316 models, with ERA-5 breaking down later than the ensemble mean but being located well
317 within the model range. The ensemble mean CAB extent peaks at the beginning of October,
318 consistent with the discontinuity width presented by Howard and Washington (2019) (their
319 Figure 5). The reanalysis spread in the seasonal cycles of these metrics is approximately
320 half of the model spread.

321 Based on the above analysis we conclude that the CAB is well represented in most of the
322 climate models considered, with the exception being CanESM2. We therefore proceed to
323 study the change in the CAB between present day and future climate models, and to assess
324 the impact of this change on rainfall in southern Africa under the RCP8.5 scenario.

325 *b. Future Change and Rainfall Implications*

326 In this section, we explore how the CAB changes in the future and whether these changes
327 are linked to projected southern African drying. Figure 6 shows the difference, in each
328 model, between the CAB latitude, frequency and extent in the RCP8.5 end of 21st century
329 simulation and in the historical end of 20th century simulation. The main change is an
330 increase in the CAB frequency from October to December, peaking at approximately 25%
331 in GFDL-CM3 and averaging to 13% in the ensemble mean. This frequency increase is
332 accompanied by a northward shift in CAB latitude on average of 0.7°. These changes are
333 significant relative to natural variability in between 11 and 15 of the 18 models across the
334 three months, as shown in the bottom panel of Figure 6. This indicates that the gradual
335 southward progression and seasonal frequency decline of the CAB is delayed in most climate
336 models, and so the CAB becomes more frequent towards the end of the season. Further
337 analysis (not shown) indicates that the delay in CAB breakdown is approximately half a
338 month. During this period, there is an increase in the CAB extent, which is significantly
339 different from 0 as compared to model spread at the $p < 0.05$ level in November and
340 December, and compared to natural variability in 12 models.

341 CAB frequency is also decreased in mid-August in most models and the ensemble mean.
342 This is the same period when the CAB frequency was not well represented in Figure 5. This
343 frequency decline may be related to the anomalous representation of the CAB in August.

344 Most models return to displaying historical CAB frequencies by September, with the ex-
345 ception of CanESM2, whose CAB was shown earlier to be poorly represented in historical
346 simulations.

347 Howard and Washington (2019) found that the interannual CAB frequency was anti-
348 correlated with precipitation between 10° and 15°S in October, November and December.
349 Since the October-December CAB frequency increases in most CMIP5 models considered
350 in this study, it seems plausible that this increase may be linked to the projected rainfall
351 decline present in most models. In order to explore this further, we decompose daily OND
352 rainfall at each grid-cell into three components:

- 353 1. North of CAB rain: rain that fell at a grid-cell that was in the same longitude band as
354 an identified CAB dryline, with the grid-cell located to the north of the dryline;
- 355 2. South of CAB rain: rain that fell at a grid-cell that was in the same longitude band as
356 an identified CAB dryline, with the grid-cell located to the south of the dryline; and
- 357 3. CAB breakdown rain: rain that fell at a grid-cell for which no CAB drylines were
358 detected in the same longitude band.

359 The top row of Figure 7 shows the decomposition of the historical climatological mean
360 OND rainfall into these three categories, as a function of latitude and averaged over lon-
361 gitudes between 20° and 30°S. As predicted, the rainfall to the south of the CAB is small,
362 and is only comparable to the total rainfall at subtropical latitudes (30°-40°S). Rainfall at
363 tropical latitudes, between 0° and 15°S, is evenly distributed between the remaining two
364 categories. North of CAB rainfall is identically zero south of 18°S, as the CAB does not
365 extend south of this point.

366 The division of rainfall into these three components is based on the hypothesis, proposed
367 by Howard and Washington (2019), that the CAB largely prevents tropical rain to its south
368 and that the primary means by which spring rainfall occurs in southern Africa is a full or
369 partial breach in the CAB. Thus component (2) - rainfall south of the CAB - is expected
370 to be small and primarily of extra-tropical origin. The other components represent: (1)
371 rainfall associated with ‘Congo Air’ in the deep tropics, and (3) rainfall associated with
372 tropical temperate troughs (TTTs) and other CAB breakdown events. This decomposition
373 does not account for the fact that a grid cell associated with an elongated TTT may exist to
374 the south of a CAB grid cell due to the TTT’s diagonal structure. However, this limitation
375 does not appear to be significant, based on the calculated low magnitude of rain to the south
376 of the CAB in Figure 7.

377 Meanwhile, the middle panel of Figure 7 shows the future change of each category of
378 rainfall. The change in the total rainfall shows the familiar dipole structure, with most
379 models showing drying south of 10°S and either wetting or a comparatively low magnitude
380 of drying north of 5°S. The decomposition into rainfall classifications is enlightening: there
381 is an increase in rainfall to the north of the CAB, and a decrease in rainfall coming from the
382 CAB breakdown events. In each case the direction of change is remarkably robust between
383 models and across latitudes.

384 To provide further visualisation of the projected change, the lower panel of Figure 7 shows
385 the envelopes indicating the model spread of rainfall projections in historical (blue) and
386 RCP8.5 (red) simulations. Change in the rainfall decomposition terms is more pronounced
387 than change in the total rainfall. The green line in these figures indicates the number of
388 models which show a significant change relative to natural variability. At least 13 of the 18
389 models show a significant decline in CAB breakdown rainfall between 8° and 28° S.

390 This implies that the ensemble mean OND drying and rainfall change dipole is associated
391 with the change in the CAB frequency. The drying is fully contained within the component
392 of the rainfall that falls on CAB breakdown days, while the wetting occurs to the north
393 of the CAB. The rainfall rate per CAB break-down day and or north of CAB rainfall per
394 CAB day was also considered, but no consensus on the sign of change was apparent (not
395 shown). The projected decrease in rainfall on non-CAB days and increase in rainfall to the
396 north of the CAB is therefore directly linked to the projected increase in the frequency of
397 CAB days. The spatial patterns of the ensemble mean change of OND rainfall under this
398 decomposition, shown in the top row of Figure 8, are consistent with this conclusion.

399 Furthermore, inter-model spread of the projected CAB frequency increase explains a large
400 proportion of the projected southern African drying. This is shown in the lower panels of
401 Figure 8, which show the inter-model regression of OND model rainfall change (averaged
402 over 15° - 30°E and 5° - 25°S) against the modelled CAB frequency change. CAB frequency
403 change is averaged over November and December, the months in which the ensemble mean
404 change is significant. Before the CAB rainfall decomposition is applied, 46% of the inter-
405 model variation of total OND rainfall change is explained by inter-model variation in the
406 CAB frequency change. Variation in the rainfall decline during CAB breakdown events is
407 more strongly predicted by variation in the CAB latitude change ($R^2=0.71$). While the
408 CanESM2 data point (blue-green circle) appears to have a large degree of leverage in these
409 regressions, its exclusion did strongly not impact the significance of the results (not shown).

410 Taken together, these results imply that the OND rainfall decline signal in southern Africa
411 is largely explained by the increased frequency of the CAB, which prevents CAB breakdown
412 associated rainfall in the regions that are located to the south of the CAB. Between 5° and

413 15°S, this comes with an increase in rainfall on CAB days, as parts of this region are often
414 located to the north of the CAB.

415 **4. Tropical lows**

416 We now shift focus to tropical lows, cyclonic vortices that form in the Austral summer
417 and have been found to deliver 31% of summer rainfall to the tropical edge region (16°-
418 22°S) of southern Africa (Howard et al. 2019). Tropical lows tend to cluster in Angola and
419 western Zambia, where they form the synoptic expression of the late-summer tropical low
420 phase of the climatological Angola low (Howard and Washington 2018). This section first
421 examines the representation of tropical lows in 18 CMIP5 models. We then consider their
422 contribution to precipitation and future change.

423 *a. Representation in Historical Climate Models*

424 In order to evaluate the representation of tropical lows in CMIP5 models, we first consider
425 climatological spatial distributions of tropical low locations, shown in Figure 9. From this
426 figure, it is evident that most models get the broad shape of the distribution of tropical
427 lows correct, with a maximum occurring in eastern Angola, the locus of the Angola tropical
428 low. There is a wide range in the number of strong tropical low events per year. Most
429 models show a lower count of tropical low days per year than the MERRA2 and ERA-5
430 reanalyses, while ERA-Interim is roughly in the middle of the model distribution. This
431 stands in contrast to the findings of Munday and Washington (2017), who report that the
432 geopotential height anomaly associated with the Angola low is over-represented in CMIP5
433 models, although they did not consider ERA-5 or MERRA-2 for comparison. However,
434 we do find that two models that have the most prevalent tropical lows (ACCESS1.3 and

435 GFDL-ESM2G) also had strong geopotential height anomalies according to Munday and
436 Washington (2017). The spread of tropical low characteristics between the three reanalysis
437 products was studied in detail by Howard et al. (2019), and is typically reduced compared
438 to the model spread.

439 The tropical low latitudes are shifted overly southwards towards the western edge of the
440 Namibian Caprivi strip (18°S, 20°E) in most models, notably BNU-ESM, CNRM-CM5,
441 inmcm4, NorESM1-M and HadGEM2-CC. The number of tropical lows per day is notably
442 low in IPSL-CM5A-LR and inmcm4. BNU-ESM and HadGEM2-ES show an overly strong
443 peak at 20°E, with very few tropical lows occurring outside the location of the Angola
444 peak. For BNU-ESM, this is also clear from Figure 3, where the track longitudes are largely
445 confined to 18° - 23°E. The biases of the spatial distribution of tropical lows in these climate
446 models relative to ERA-5 reanalysis, and their significance relative to natural variability
447 over the 30-year time period, are shown in Supplementary Figure S3.

448 Figure 10 shows the normalized distributions of four key properties of tropical lows: their
449 longevities, latitudes, zonal velocities and T63 filtered vorticity. The southward shift of the
450 tropical lows in CMIP5 models as compared to reanalysis is more clear from the latitude
451 distribution sub-plot. Based on the distributions of longevity and zonal velocity, models may
452 be divided into two groups: those with relatively more short-lived (<8 days) and relatively
453 fewer long-lived tropical lows (10-20 days) than the reanalysis products, and those with
454 fewer short-lived and more long-lived tropical lows. Those models in the first category
455 tend to have a wider distribution of zonal velocities, with faster track speeds, while those
456 in the second category have a greater proportion of stationary lows concentrated around
457 0 m/s. The first category therefore contains a greater proportion of transient events that
458 move off into the Atlantic Ocean, and the second contains a greater proportion of stationary

459 Angola tropical lows. Typical extreme cases for each category are CNRM-CM5 and GFDL-
460 ESM2G. Examining Figure 3 reveals a consistent story: for the case study year CNRM-CM5
461 is dominated by transient events (diagonal lines) while GFDL-ESM2G contains 4-5 long-
462 lived events that meander across the continent and are frequency stationary, as well as
463 some smaller events that are both stationary and transient. The distributions of the filtered
464 vorticity largely follow that of reanalysis. Biases in all these quantities are significant relative
465 to natural variability in at least 12 out of the 17 models considered.

466 The top right panel of Figure 10 shows the number of tropical low days per year. This
467 metric reflects the overall magnitude of the signal in Figure 3 discussed earlier. The models
468 with the lowest values (IPSL-CM5A-LR and inmcm4) also show a higher proportion of
469 tropical lows just below the vorticity cut-off in the lower left panel of Figure 10.

470 Rainfall is attributed to tropical lows under the assumption that all rainfall that falls within
471 5 degrees of the centroid of a tropical low is associated with that tropical low. Rainfall is
472 decomposed into a tropical low portion and a remainder portion. Howard et al. (2019) found
473 that 70% of rainfall in south west Angola and 31% of rainfall across the tropical edge region
474 (16° - 22° S) was attributable to tropical lows. The spatial pattern of rainfall attribution
475 for CMIP5 models is shown in Figure 11, and the overall proportion of rainfall attributed
476 to tropical lows in each model between 15° - 30° E and 10° - 25° S is shown in the lower right
477 panel of Figure 10. We find that approximately 30% - 60% of rainfall over southern Africa
478 is associated with tropical lows between these latitudes. The spatial patterns of rainfall
479 attribution match well with those found by Howard et al. (2019) (reproduced here in lower
480 panels of Figure 11). The biases of these spatial patterns relative to ERA-5 reanalysis, and
481 their significance relative to natural variability over the 30-year time period, are shown in
482 Supplementary Figure S4.

483 There are some differences between tropical lows in reanalysis products and in CMIP5
484 models, including latitude and longevity distributions, and there is a wide distribution across
485 models in the mean number of strong tropical low days per year. However, tropical lows are
486 consistently present in each model with key statistics varying by less than 20%. We therefore
487 conclude that they are sufficiently resolved to examine projected tropical low changes and
488 how those changes impact southern African precipitation projections.

489 *b. Future Change and Rainfall Implications*

490 The overall trend in the spatial distribution of tropical lows between end of 21st century
491 RCP8.5 and end of 20th century historical simulations is a decrease in tropical low frequency
492 and in some cases a northward shift, as is shown in Figure 12. Some models, including AC-
493 CESS1.0, HadGEM2-CC, HadGEM2-ES and GFDL-CM3, show a sharp decline in tropical
494 lows exceeding 1 tropical low day per $2^\circ \times 2^\circ$ box per year that is restricted to the location of
495 the peak of their historical tropical low locations. Northward shifts are evident in CanESM2,
496 IPSL-CM5A-LR and MPI-ESM-LR. Only MPI-ESM-MR shows an increase in tropical low
497 frequency. Despite many models showing similar overall patterns in tropical low decline, the
498 spatial pattern of change and the location of statistically significant changes varies widely
499 across the models. The ensemble mean exhibits an overall 15% decline in the number of
500 tropical low days that occur in each year.

501 Correspondingly, the spatial pattern of rainfall change between December and February,
502 the main tropical low months, shows a high degree of variation between models, consistent
503 with Lazenby et al. (2018). Filled green and purple contours show wetting and drying of the
504 overall seasonal mean rainfall in each model in Figure 13. These are overlain by contours,
505 in black and red, of the wetting and drying of the component of the rainfall attributed

506 to tropical lows. Changes which were not significant compared to natural variability at a
507 $p < 0.05$ level were masked. It is evident that all the land-based local maxima and minima
508 of total rainfall change located between 10° and 25°S correspond to an associated maxima or
509 minima in tropical low rainfall change. Comparing with Figure 12, these changes correspond
510 with spatial changes in the frequency of tropical lows.

511 The ensemble mean tropical low rainfall change in this region (Figure 13, lower right panel)
512 also corresponds to the ensemble mean tropical low spatial distribution change (Figure 12,
513 lower right panel), with a decrease along 18°S centered south east Angola and an increase
514 further north. The spatial pattern of total rainfall decline maps accurately onto the spatial
515 pattern of tropical low rainfall decline in southern Angola and northern Namibia. However,
516 the rainfall increase to the north of this region has its maximum further north in the Congo
517 and is likely delivered by other synoptic systems.

518 In order to quantify the relationship between changes in rainfall and tropical low frequency,
519 the Pearson's r coefficient of the spatial correlation between projected rainfall change and
520 tropical low frequency change between $5^\circ - 25^\circ\text{S}$ for all land points is shown in the top row
521 of Figure 14. The correlation for overall rainfall is low (typically 0.1 - 0.3) but consistently
522 positive in all but two models. The correlation for the tropical low rainfall component is
523 higher, with values averaging around 0.4. There is no consistent signal in the direction of
524 correlation between the remaining rainfall pattern change and the tropical low distribution
525 change. In this manner, the divergence in model rainfall projections in DJF over tropical
526 southern Africa is linked to the uncertainty in the spatial response of tropical lows to climate
527 change.

528 Averaging over land points in the region from $5^\circ - 25^\circ\text{S}$, the projected frequency change
529 in tropical lows is a good predictor of the inter-model spread of rainfall change ($r=0.58$,

530 $p=0.015$). This is indicated in the regression shown in Figure 14 (lower left panel). The
531 decomposition into rainfall associated with tropical lows and a remainder component (lower
532 center and right panels of Figure 14) indicates that this influence of tropical lows is direct, as
533 the change in tropical low rainfall is significantly correlated with the change in tropical lows,
534 and the change in the remainder term is not. Therefore, the spread in future projections of
535 tropical lows is a major contributor to the spread of rainfall predictions in DJF over southern
536 Africa.

537 **5. Discussion**

538 *a. Remarks on the Congo Air Boundary*

539 We have found that the CAB is well represented in CMIP5 models, and that its projected
540 frequency increase is able to distinguish between models that show strong and weak declines
541 in OND rainfall south of 10°S . In this section, we discuss the implications of the historical
542 representation of the CAB, and compare our results to other studies of the OND rainfall
543 decline.

544 The accuracy of historical representation of the CAB in CMIP5 models is reasonable,
545 despite the perpendicular width of the CAB being of order 100 km (Howard and Washington
546 2019), below the resolution of most CMIP5 models. The southward displacement of the
547 CAB between August and December is roughly 8 degrees of latitude, which in the coarsest
548 models is equivalent to 4 grid cells, and yet the rate of the CAB's progression is very similar
549 across models. This suggests that representation of the CAB, and its seasonal progression,
550 is controlled by a process that climate models do not struggle to simulate, and so is not
551 controlled by processes that act at the grid box scale. As with the tropical rainbelt globally,

552 the seasonal progression is clearly associated with the progression of the latitude of maximum
553 solar insolation. Meanwhile, the sharp gradients in humidity bring to mind bifurcations into
554 dry and moist convective states observed in idealized radiative convective equilibrium models
555 (e.g., Emanuel et al. 2014).

556 We have found that projections of CAB frequency have different consequences north and
557 south of the climatological CAB. The relationship between the CAB frequency and rainfall
558 south of the CAB's climatological position is an intuitive one. In this region, saturation is
559 rarely achieved when the CAB is present, unless extra-tropical processes dominate. Most
560 rainfall comes from CAB breakdown events. When the gradual seasonal CAB breakdown
561 is delayed, as in the future model projections, there are fewer rainy days in this region,
562 and hence less rain. Meanwhile, there is an overall increase in rainfall to the north of the
563 climatological CAB. However, this increase is not limited to the location of the CAB, as
564 OND rainfall is projected to increase across much of equatorial Africa (Creese et al. 2019).
565 Therefore, there is a consistent projected increase in rainfall in locations that are generally
566 located the north of the CAB, but this is not necessarily driven by the corresponding pro-
567 jected increase in CAB frequency. The contrasting impacts that the CAB frequency has to
568 its north and south are important for determining the precise location of projected rainfall
569 decline. Rainfall to the south of the mean CAB position is projected to decline due to the
570 projected increase in CAB frequency, while rainfall to the north is projected to increase.
571 Therefore, the CAB may be expected to set the location of the boundary of rainfall decline.

572 The work presented here is consistent with previous studies of rainfall projections over
573 southern Africa. Dunning et al. (2018) found that the seasonal progression of the African
574 rain belt is tied up in the strengths of the Saharan and Angola heat lows, both of which
575 are projected to intensify in a warmer world. Munday and Washington (2019) found a

576 similar result, that models with a deeper future Angola heat low showed a higher intensity
577 of drying, while Cook and Vizy (2013) observed a strengthening of the heat low in regional
578 climate model simulations. The Angola heat low is intrinsically linked to the CAB (Howard
579 and Washington 2019), being consistently located approximately 1° south of the CAB and
580 sharing circulation features. Therefore an increase in the climatological CAB frequency
581 corresponds to an increase in the heat low intensity.

582 By applying the Chadwick et al. (2013) decomposition, Lazenby et al. (2018) attributed
583 the OND rainfall change to dynamic rather than thermodynamic changes, associated with
584 spatial shifts in the pattern of convective mass fluxes. In the context of this methodology, it
585 is useful to consider the atmosphere to the north of the CAB and during CAB breakdown
586 events as capable of deep convection, and to the south of the CAB as incapable of deep
587 convection. The increased CAB frequency corresponds to a decrease in the proportion of
588 the time that convection may occur in the region south of 10°S , and so is associated with a
589 shift in deep convection away from southern Africa.

590 Figures 3(f-g) in Lazenby et al. (2018) also demonstrated that there was a decrease in
591 near surface relative humidity between 10° and 20°S , but that this did not contribute to
592 the overall precipitation change budget. This finding underscores the fundamental concept
593 outlined by the CAB: that the southern African atmosphere during the Austral spring is often
594 characterized at any instant by a dichotomy of states: one that is severely moisture limited
595 and one that is close to saturated, with very little in between (Howard and Washington
596 2019). In such a scenario, small thermodynamic perturbations have less potential to change
597 the likelihood of convection than small dynamical perturbations. This is because a dynamical
598 perturbation may move the moist airmass into, or away from a given location, drastically
599 changing the likelihood of convection at that spot. Meanwhile, a small change in saturation

600 temperature is unlikely to change the likelihood of convection if the atmosphere is either
601 severely dry or not at all moisture limited.

602 *b. Remarks on Tropical lows*

603 Uncertainty in future projections of tropical lows in southern Africa has been identified
604 as a source of the uncertainty and broad model spread in rainfall projections in this region
605 during the main rainy season. This uncertainty derives from variations in the changes of the
606 climatological tropical low spatial distribution, however some robust changes are present, as
607 discussed below.

608 The historical spatial distribution of tropical lows features a southward bias as compared
609 to reanalysis. Models show a greater proportion of tropical lows centered near 18°S and
610 too few located around 15°S. This bias is consistent with other studies of the historical
611 CMIP5 rainfall bias over southern Africa. An interannual southward shift in the Angola low
612 has been associated with an increase in rainfall over subtropical southern Africa (Pascale
613 et al. 2019; Crétat et al. 2018), consistent with the direction of the rainfall bias (Lazenby
614 et al. 2016). Furthermore, Munday and Washington (2017) found a correlation between the
615 magnitude of this wet bias and the strength of the Angola low, which they found was overly
616 intense in most models. They also found that the climatological position of the Angola low
617 was shifted towards the Angola-Namibia border in many models.

618 Despite differences in the patterns, there is a consensus in all but one model of overall
619 tropical low decline south of 15°S. This is reflected in the ensemble mean of both precipitation
620 and tropical low location shifts. A large minority of models also show a marked increase in
621 tropical lows north of this line, signifying a northward shift. However, this change is less
622 robust than the decline further south. A northward shift and overall decline of tropical low

623 location mirrors the characteristic response of tropical lows to El Niño events (Howard et al.
624 2019; Pascale et al. 2019).

625 Lazenby et al. (2018) proposed that the diverse range of future projections in DJF is
626 associated with inter-model differences in the SST changes in the Indian and Atlantic Oceans.
627 Since interannual variability of the Angola low, which in late summer is the climatological
628 expression of tropical lows, is sensitive to SSTs in these oceans (Pascale et al. 2019), it is
629 likely that variability in SST projections may lead to variability in tropical low distributions,
630 which in turn lead to the spread of projected rainfall changes.

631 **6. Conclusion**

632 The CMIP5 ensemble predicts a drying trend in both spring and summer in southern
633 Africa. Spring drying is robust across all models, and is associated with a delay in the wet
634 season onset (Dunning et al. 2018). Such delays would cause a shortening of the growing
635 season, impacting regional agriculture and food security (Lobell et al. 2008; Schlenker and
636 Lobell 2010). Model projections in the summer are more divergent and the ensemble mean
637 drying trend in this season is less robust. However, rainfall changes in this season would be
638 equally disruptive to the local economy. For this reason, it is imperative that the mechanisms
639 of future rainfall change demonstrated by CMIP5 models are well understood.

640 The present study has placed the spring and summer projected rainfall change in the
641 context of two classes of weather events, tropical lows and the CAB. These features are
642 predominant in each respective season and are sufficiently well resolved in the climate models.
643 By doing so, we have attributed model consensus on spring drying to increases in CAB
644 frequency and latitude, and the lack of model consensus on summer rainfall change to
645 uncertainty in the tropical low response to a warmer world. This work provides crucial

646 context for the projected changes and grounds changes to the local climate in meteorological
647 theory.

648 We have found that the spring drying trend is strongly correlated across models with an
649 increased frequency in the CAB. This delayed breakdown causes an increase in its average
650 frequency between October and December of approximately 13%. Model consensus on its
651 projected change agree that the CAB will be located $0.5^\circ - 1^\circ$ further north and its gradual
652 seasonal decline will occur half a month later at the end of 21st century than the 20th under
653 the RCP8.5 scenario. These changes are significant as against internal variability in 12 - 15
654 of the 18 models. Therefore, we strongly advocate for further research into this understudied
655 feature of the climate system, particularly in the form of observational field campaigns.

656 Tropical lows, which make up the synoptic expression of the Angola low in the southern
657 African summer, show more model spread in their future change, particularly when con-
658 sidering small-scale spatial shifts. This increased model uncertainty is a contributor to the
659 divergence of DJF rainfall projections in southern Africa. However, despite spatial differ-
660 ences, a statistically significant decline in tropical low frequency south of 15°S is present in
661 11 models, with an overall ensemble mean decline of 10%. The response of tropical lows to
662 future warming will be important for rainfall change in this region.

663 *Acknowledgments.* This work has been generously supported by the Origin Founda-
664 tion John Monash Scholarship and by the Future Climate for Africa UMFULA project,
665 with financial support from the U.K. Natural Environment Research Council (NERC),
666 NE/M020207/1, and the U.K. Government's Department for International Development
667 (DfID). The GCM data used in this study were made available through the Earth Sys-
668 tem Grid Federation (ESGF) Peer-to-Peer system (<https://pcmdi.llnl.gov/search/>

669 cmip5/). Reanalysis data used in this analysis were provided by the Copernicus Cli-
670 mate Change Service (<https://cds.climate.copernicus.eu/cdsapp#!/home>), the Euro-
671 pean Centre for Medium Range Weather Forecasts ([https://apps.ecmwf.int/datasets/
672 data/interim-full-daily/levtype=pl/](https://apps.ecmwf.int/datasets/data/interim-full-daily/levtype=pl/)) and NASA ([https://disc.sci.gsfc.nasa.
673 gov/daac-bin/FTPSubset.pl](https://disc.sci.gsfc.nasa.gov/daac-bin/FTPSubset.pl)). Color maps were sourced from cmocean ([https://
674 matplotlib.org/cmocean/](https://matplotlib.org/cmocean/)). We thank Kevin Hodges for access to TRACK and Paul-
675 Arthur Monerie for assistance regarding decadal variability.

676 References

- 677 Aloysius, N. R., J. Sheffield, J. E. Sainers, H. Li, and E. F. Wood, 2016: Evaluation of
678 historical and future simulations of precipitation and temperature in central Africa from
679 CMIP5 climate models. *Journal of Geophysical Research: Atmospheres*, **121** (1), 130–152,
680 doi:10.1002/2015JD023656, URL <http://doi.wiley.com/10.1002/2015JD023656>.
- 681 Baray, J., S. Baldy, R. Diab, and J. Cammas, 2003: Dynamical study of a tropical cut-off
682 low over south africa, and its impact on tropospheric ozone. *Atmospheric Environment*,
683 **37** (11), 1475 – 1488, doi:[https://doi.org/10.1016/S1352-2310\(02\)00999-8](https://doi.org/10.1016/S1352-2310(02)00999-8), URL [http://
684 //www.sciencedirect.com/science/article/pii/S1352231002009998](http://www.sciencedirect.com/science/article/pii/S1352231002009998).
- 685 Bengtsson, L., K. I. Hodges, M. Esch, N. Keenlyside, L. Kornblueh, J. J. Luo, and T. Ya-
686 magata, 2007: How may tropical cyclones change in a warmer climate? *Tellus, Series*
687 *A: Dynamic Meteorology and Oceanography*, **59 A** (4), 539–561, doi:10.1111/j.1600-0870.
688 2007.00251.x, URL <https://doi.org/10.1111/j.1600-0870.2007.00251.x>.
- 689 Canny, J., 1986: A Computational Approach to Edge Detection. *IEEE Transactions on*
690 *Pattern Analysis and Machine Intelligence*, **8** (6), 679–698, doi:10.1109/TPAMI.1986.

691 4767851, URL <https://doi.org/10.1109/TPAMI.1986.4767851>.

692 Chadwick, R. S., I. Boutle, and G. Martin, 2013: Spatial patterns of precipitation change in
693 CMIP5: Why the rich do not get richer in the tropics. *Journal of Climate*, **26** (11),
694 3803–3822, doi:10.1175/JCLI-D-12-00543.1, URL <https://journals.ametsoc.org/doi/10.1175/JCLI-D-12-00543.1>.

696 Chou, C., J. D. Neelin, C. A. Chen, and J. Y. Tu, 2009: Evaluating the "rich-get-richer"
697 mechanism in tropical precipitation change under global warming. *Journal of Climate*,
698 **22** (8), 1982–2005, doi:10.1175/2008JCLI2471.1, URL <https://journals.ametsoc.org/doi/pdf/10.1175/2008JCLI2471.1>.

700 Conway, D., and Coauthors, 2015: Climate and southern Africa's water-energy-food nexus.
701 *Nature Climate Change*, **5** (9), 837–846, doi:10.1038/nclimate2735, URL <https://doi.org/10.1038/nclimate2735>.

703 Cook, C., C. J. Reason, and B. C. Hewitson, 2004: Wet and dry spells within particularly
704 wet and dry summers in the South African summer rainfall region. *Climate Research*,
705 **26** (1), 17–31, doi:10.3354/cr026017, URL <https://doi.org/10.3354/cr026017>.

706 Cook, K. H., and E. K. Vizy, 2013: Projected changes in East African rainy seasons. *Journal*
707 *of Climate*, **26** (16), 5931–5948, doi:10.1175/JCLI-D-12-00455.1, URL <https://doi.org/10.1175/JCLI-D-12-00455.1>.

709 Creese, A., R. Washington, and C. Munday, 2019: The Plausibility of September–November
710 Congo Basin Rainfall Change in Coupled Climate Models. *Journal of Geophysical Re-*
711 *search: Atmospheres*, **124** (11), 5822–5846, doi:10.1029/2018JD029847, URL <https://onlinelibrary.wiley.com/doi/abs/10.1029/2018JD029847>.

713 Crétat, J., B. Pohl, B. Dieppois, S. Berthou, and J. Pergaud, 2018: The Angola Low:
714 relationship with southern African rainfall and ENSO. *Climate Dynamics*, **52** (4), 1783–
715 1803, doi:10.1007/s00382-018-4222-3, URL <https://doi.org/10.1007/s00382-018-4222-3>.

716 Dare, R. A., N. E. Davidson, and J. L. McBride, 2012: Tropical Cyclone Contribution
717 to Rainfall over Australia. *Monthly Weather Review*, **140** (11), 3606–3619, doi:10.1175/
718 MWR-D-11-00340.1, URL <https://journals.ametsoc.org/doi/10.1175/MWR-D-11-00340.1>.
719 1.

720 Dunning, C. M., E. C. Black, and R. P. Allan, 2018: Later wet seasons with more intense
721 rainfall over Africa under future climate change. *Journal of Climate*, **31** (12), JCLI-D-18–
722 0102.1, doi:10.1175/JCLI-D-18-0102.1, URL <https://doi.org/10.1175/JCLI-D-18-0102.1>.

723 Emanuel, K., A. A. Wing, and E. M. Vincent, 2014: Radiative-convective instability. *Journal*
724 *of Advances in Modeling Earth Systems*, **6** (1), 75–90, doi:10.1002/2013MS000270, URL
725 <https://doi.org/10.1002/2013MS000270>.

726 Hachigonta, S., C. J. Reason, and M. Tadross, 2008: An analysis of onset date and rainy
727 season duration over Zambia. *Theoretical and Applied Climatology*, **91** (1-4), 229–243,
728 doi:10.1007/s00704-007-0306-4, URL <https://doi.org/10.1007/s00704-007-0306-4>.

729 Held, I. M., and B. J. Soden, 2006: Robust Responses of the Hydrological Cycle to Global
730 Warming. *Journal of Climate*, **19** (11), 5686–5699, URL [https://journals.ametsoc.org/
731 doi/10.1175/JCLI3990.1](https://journals.ametsoc.org/doi/10.1175/JCLI3990.1).

732 Hodges, K. I., 1994: A General Method for Tracking Analysis and its Applica-
733 tion to Meteorological Data. *Monthly Weather Review*, **122** (11), 2573–2586, doi:

734 10.1175/1520-0493(1994)122<2573:AGMFTA>2.0.CO;2, URL [https://doi.org/10.1175/1520-0493\(1994\)122<2573:AGMFTA>2.0.CO;2](https://doi.org/10.1175/1520-0493(1994)122<2573:AGMFTA>2.0.CO;2),
735 1520-0493(1994)122<2573:AGMFTA>2.0.CO;2.

736 Hodges, K. I., 1999: Adaptive Constraints for Feature Tracking. *Monthly Weather Review*,
737 **127**, 1362–1373, doi:10.1175/1520-0493(1999)127<1362:ACFFT>2.0.CO;2, URL [https://doi.org/10.1175/1520-0493\(1999\)127<1362:ACFFT>2.0.CO;2](https://doi.org/10.1175/1520-0493(1999)127<1362:ACFFT>2.0.CO;2).
738 doi.org/10.1175/1520-0493(1999)127<1362:ACFFT>2.0.CO;2.

739 Hodges, K. I., A. Cobb, and P. L. Vidale, 2017: How well are tropical cyclones repre-
740 sented in reanalysis datasets? *Journal of Climate*, **30** (14), 5243–5264, doi:10.1175/
741 JCLI-D-16-0557.1, URL <https://doi.org/10.1175/JCLI-D-16-0557.1>.

742 Howard, E., and R. Washington, 2018: Characterizing the synoptic expression of the angola
743 low. *Journal of Climate*, **31** (17), 7147–7165, doi:10.1175/JCLI-D-17-0017.1, URL <https://doi.org/10.1175/JCLI-D-17-0017.1>,
744 [//doi.org/10.1175/JCLI-D-18-0017.1](https://doi.org/10.1175/JCLI-D-18-0017.1).

745 Howard, E., and R. Washington, 2019: Drylines in Southern Africa: Rediscovering the
746 Congo Air Boundary. *Journal of Climate*, **32**, 8223–8242, URL [https://doi.org/10.1175/
747 JCLI-D-19-0437.1](https://doi.org/10.1175/JCLI-D-19-0437.1).

748 Howard, E., R. Washington, and K. I. Hodges, 2019: Tropical lows in southern Africa:
749 tracks, rainfall contributions and the role of ENSO. *Journal of Geophysical Research:
750 Atmospheres* (*in press*).

751 James, R., and R. Washington, 2013: Changes in African temperature and precipitation
752 associated with degrees of global warming. *Climatic Change*, **117** (4), 859–872, doi:10.
753 1007/s10584-012-0581-7, URL <https://doi.org/10.1007/s10584-012-0581-7>.

- 754 Jiang, Y., L. Zhou, C. J. Tucker, A. Raghavendra, W. Hua, Y. Y. Liu, and J. Joiner, 2019:
755 Widespread increase of boreal summer dry season length over the congo rainforest. *Nature*
756 *Climate Change*, **9**, 617–622, URL <https://doi.org/10.1038/s41558-019-0512-y>.
- 757 Khouakhi, A., G. Villarini, and G. A. Vecchi, 2017: Contribution of tropical cyclones to rain-
758 fall at the global scale. *Journal of Climate*, **30** (1), 359–372, doi:10.1175/JCLI-D-16-0298.
759 1, URL <https://journals.ametsoc.org/doi/10.1175/JCLI-D-16-0298.1>.
- 760 Kniveton, D. R., R. Layberry, C. J. R. Williams, and M. Peck, 2009: Trends in the start of
761 the wet season over Africa. *International Journal of Climatology*, **29** (9), 1216–1225, doi:
762 10.1002/joc.1792, URL <https://rmets.onlinelibrary.wiley.com/doi/abs/10.1002/joc.1792>,
763 <https://rmets.onlinelibrary.wiley.com/doi/pdf/10.1002/joc.1792>.
- 764 Lavender, S. L., and D. J. Abbs, 2013: Trends in Australian rainfall: Contribution of
765 tropical cyclones and closed lows. *Climate Dynamics*, **40** (1-2), 317–326, doi:10.1007/
766 s00382-012-1566-y, URL <https://doi.org/10.1007/s00382-012-1566-y>.
- 767 Lazenby, M. J., M. C. Todd, R. S. Chadwick, and Y. Wang, 2018: Future precipitation
768 projections over central and Southern Africa and the adjacent Indian Ocean: What causes
769 the changes and the uncertainty? *Journal of Climate*, **31** (12), 4807–4826, doi:10.1175/
770 JCLI-D-17-0311.1, URL <https://doi.org/10.1175/JCLI-D-17-0311.1>.
- 771 Lazenby, M. J., M. C. Todd, and Y. Wang, 2016: Climate model simulation of the South
772 Indian Ocean Convergence Zone: Mean state and variability. *Climate Research*, **68** (1),
773 59–71, doi:10.3354/cr01382, URL <https://doi.org/10.3354/cr01382>.
- 774 Leroux, M., 2001: *The climate of tropical Africa*, Vol. 3-9. Springer, 39–45 pp.

775 Lobell, D. B., M. B. Burke, C. Tebaldi, M. D. Mastrandrea, W. P. Falcon, and R. L. Naylor,
776 2008: Prioritizing Climate Change Adaptation Needs for Food Security in 2030. *Science*, **319**
777 **(5863)**, 607–610, doi:10.1126/science.1152339, URL [https://doi.org/10.1126/](https://doi.org/10.1126/science.1152339)
778 [science.1152339](https://doi.org/10.1126/science.1152339).

779 Munday, C., and R. Washington, 2017: Circulation Controls on Southern African Precipitation
780 in Coupled Models: The Role of the Angola Low. *Journal of Geophysical Research: Atmospheres*, **122**,
781 1–17, doi:10.1002/2016JD025736, URL [https://doi.org/10.](https://doi.org/10.1002/2016JD025736)
782 [1002/2016JD025736](https://doi.org/10.1002/2016JD025736).

783 Munday, C., and R. Washington, 2019: Controls on the diversity in climate model projections
784 of early summer drying over Southern Africa. *Journal of Climate*, **32**, 3707–
785 3725, doi:10.1175/JCLI-D-18-0463.1, URL [http://journals.ametsoc.org/doi/10.1175/](http://journals.ametsoc.org/doi/10.1175/JCLI-D-18-0463.1)
786 [JCLI-D-18-0463.1](http://journals.ametsoc.org/doi/10.1175/JCLI-D-18-0463.1).

787 Pascale, S., B. Pohl, S. B. Kapnick, and H. Zhang, 2019: On the Angola Low Interannual
788 Variability and Its Role in Modulating ENSO Effects in Southern Africa. *Journal of Climate*, **32**
789 **(15)**, 4783–4803, doi:10.1175/jcli-d-18-0745.1, URL [https://doi.org/10.1175/](https://doi.org/10.1175/jcli-d-18-0745.1)
790 [JCLI-D-18-0745.1](https://doi.org/10.1175/jcli-d-18-0745.1).

791 Rastogi, D., M. Ashfaq, L. R. Leung, S. Ghosh, A. Saha, K. I. Hodges, and K. Evans, 2018:
792 Characteristics of Bay of Bengal Monsoon Depressions in the 21st Century. *Geophysical Research Letters*, **45**
793 **(13)**, 6637–6645, doi:10.1029/2018GL078756, URL [https://doi.org/](https://doi.org/10.1029/2018GL078756)
794 [10.1029/2018GL078756](https://doi.org/10.1029/2018GL078756).

795 Reason, C. J., and D. Jagadheesha, 2005: A model investigation of recent ENSO impacts
796 over southern Africa. *Meteorology and Atmospheric Physics*, **89** **(1-4)**, 181–205, doi:10.
797 [1007/s00703-005-0128-9](https://doi.org/10.1007/s00703-005-0128-9), URL <https://doi.org/10.1007/s00703-005-0128-9>.

798 Rowell, D. P., and R. S. Chadwick, 2018: Causes of the uncertainty in projections of
799 tropical terrestrial rainfall change: East Africa. *Journal of Climate*, **31** (15), 5977–
800 5995, doi:10.1175/JCLI-D-17-0830.1, URL [http://journals.ametsoc.org/doi/10.1175/
801 JCLI-D-17-0830.1](http://journals.ametsoc.org/doi/10.1175/JCLI-D-17-0830.1).

802 Sardeshmukh, P. D., and B. J. Hoskins, 1988: The Generation of Global Rotational Flow
803 by Steady Idealized Tropical Divergence. *Journal of the Atmospheric Sciences*, **45** (7),
804 1228–1251, doi:10.1175/1520-0469(1988)045<1228:TGOGRF>2.0.CO;2, URL [https://doi.
805 org/10.1175/1520-0469\(1988\)045\(1228:TGOGRF\)2.0.CO;2](https://doi.org/10.1175/1520-0469(1988)045(1228:TGOGRF)2.0.CO;2).

806 Scheff, J., and D. Frierson, 2012a: Twenty-First-Century multimodel subtropical precipi-
807 tation declines are mostly midlatitude shifts. *Journal of Climate*, **25** (12), 4330–4347,
808 doi:10.1175/JCLI-D-11-00393.1, URL <https://doi.org/10.1175/JCLI-D-11-00393.1>.

809 Scheff, J., and D. M. W. Frierson, 2012b: Robust future precipitation declines in CMIP5
810 largely reflect the poleward expansion of model subtropical dry zones. *Geophysical Re-
811 search Letters*, **39** (17), 1–6, doi:10.1029/2012GL052910, URL [https://doi.org/10.1029/
812 2012GL052910](https://doi.org/10.1029/2012GL052910).

813 Schlenker, W., and D. B. Lobell, 2010: Robust negative impacts of climate change on African
814 agriculture. *Environmental Research Letters*, **5** (1), doi:10.1088/1748-9326/5/1/014010,
815 URL <https://doi.org/10.1088/1748-9326/5/1/014010>.

816 Taljaard, J. J., 1953: The mean circulation in the lower troposphere over Southern Africa.
817 *South African Geographical Journal*, **35** (1), 33–45, doi:10.1080/03736245.1953.10559299,
818 URL <https://doi.org/10.1080/03736245.1953.10559299>.

- 819 Taljaard, J. J., 1972: Synoptic Meteorology of the Southern Hemisphere. *Meteorology of*
820 *the Southern Hemisphere*, C. W. Newton, Ed., American Meteorological Society, Boston,
821 chap. 8, 139–213.
- 822 Taljaard, J. J., 1986: Change of rainfall distribution and circulation patterns over Southern
823 Africa in summer. *Journal of Climatology*, **6**, 579–592, URL [https://doi.org/10.1002/joc.](https://doi.org/10.1002/joc.3370060602)
824 3370060602.
- 825 Torrance, J. D., 1979: Upper windflow patterns in relation to rainfall in South-East Central
826 Africa. *Weather*, **34 (3)**, 106–115, doi:10.1002/j.1477-8696.1979.tb03418.x, URL <https://doi.org/10.1002/j.1477-8696.1979.tb03418.x>.
- 828 Van Heerden, J., and J. J. Taljaard, 1998: Africa and Surrounding Waters. *Meteorology of*
829 *the Southern Hemisphere*, D. J. Karoly, and D. G. Vincent, Eds., American Meteorological
830 Society, Easton, 141–174.

831 **LIST OF TABLES**

832 **Table 1.** List of CMIP5 models and reanalysis products considered in this
833 study, together with horizontal grid spacings, and an indication of
834 whether the model was used to study the CAB, tropical lows (TL) or
835 both. 40

836 TABLE 1. List of CMIP5 models and reanalysis products considered in this study, together with
837 horizontal grid spacings, and an indication of whether the model was used to study the CAB,
838 tropical lows (TL) or both.

Model Name	Institute	Horizontal Spacing	CAB	TL
bcc-csm1-1-m	Beijing Climate Center, China Meteorological Administration College of Global Change and	$1.125^\circ \times 1.125^\circ$	1	1
BNU-ESM	Earth System Science, Beijing Normal University	$2.8^\circ \times 2.8^\circ$	1	1
CanESM2	Canadian Centre for Climate Modelling and Analysis	$2.8^\circ \times 2.8^\circ$	1	1
CNRM-CM5	Centre National de Recherches Meteorologiques Commonwealth Scientific and	$1.4^\circ \times 1.4^\circ$	1	1
ACCESS1-0	Industrial Research Organisation and Bureau of Meteorology, Australia Commonwealth Scientific and	$1.25^\circ \times 1.825^\circ$	1	1
ACCESS1-3	Industrial Research Organisation and Bureau of Meteorology, Australia Commonwealth Scientific and	$1.25^\circ \times 1.825^\circ$	1	1
CSIRO-Mk3-6-0	Industrial Research Organisation in collaboration with Queensland Climate Change Centre of Excellence	$1.825^\circ \times 1.825^\circ$	1	
inmcm4	Institute for Numerical Mathematics, Moscow, Russia	$1.5^\circ \times 2.0^\circ$	1	1
IPSL-CM5A-LR	L'Institut Pierre-Simon Laplace	$1.9^\circ \times 3.75^\circ$	1	1
IPSL-CM5A-MR	L'Institut Pierre-Simon Laplace	$1.25^\circ \times 2.5^\circ$	1	1
IPSL-CM5B-LR	L'Institut Pierre-Simon Laplace	$1.9^\circ \times 3.75^\circ$	1	1
HadGEM2-CC	UK Met Office Hadley Centre	$1.25^\circ \times 1.9^\circ$	1	1
HadGEM2-ES	UK Met Office Hadley Centre	$1.25^\circ \times 1.9^\circ$	1	1

MPI-ESM-LR	Max Planck Institute for Meteorology M24	$1.8^\circ \times 1.8^\circ$	1	
MPI-ESM-MR	Max Planck Institute for Meteorology M24	$1.8^\circ \times 1.8^\circ$	1	
NorESM1-M	Norwegian Climate Centre	$1.875^\circ \times 2.5^\circ$	1	1
GFDL-CM3	NOAA/Geophysical Fluid Dynamics Laboratory	$2.0^\circ \times 2.5^\circ$	1	1
GFDL-ESM2G	NOAA/Geophysical Fluid Dynamics Laboratory	$2.0^\circ \times 2.5^\circ$	1	1
GFDL-ESM2M	NOAA/Geophysical Fluid Dynamics Laboratory	$2.0^\circ \times 2.5^\circ$	1	
CESM1-CAM5	Community Earth System Model contributor	$0.94^\circ \times 1.25^\circ$	1	
Reanalysis Name	Institute	Horizontal Spacing	CAB	TL
ERA-5	European Centre for Medium Range Forecasting	$0.25^\circ \times 0.25^\circ$	1	1
ERA-Interim	European Centre for Medium Range Forecasting	$0.75^\circ \times 0.75^\circ$	1	1
MERRA-2	NASA	$0.5^\circ \times 0.75^\circ$	1	1

839 **LIST OF FIGURES**

840 **Fig. 1.** Surface relative humidity (left panel), Canny edges (middle panel) and identified
841 CAB locations (right panel) on the 9th of September 1999 in ACCESS1.3. 44

842 **Fig. 2.** Surface relative humidity (colors) and identified CAB locations (red dots) on the
843 9th of September 1999 in each model and reanalysis product. Surface humidity
844 has been regridded to a $2^\circ \times 2^\circ$ grid using the nearest neighbor method. 45

845 **Fig. 3.** Tropical low track Hovmöller plots for each model and reanalysis product.
846 x -axis: longitude, y -axis: time. Colors indicate the T63 filtered vorticity of
847 the tropical low event, a measure of the event intensity. 46

848 **Fig. 4.** Spatial distributions of CAB and KD frequency (number of events per inter-
849 polated grid cell per year). Filled contours: CAB. Line contours: KD. Panels
850 indicate different models and reanalysis products. 47

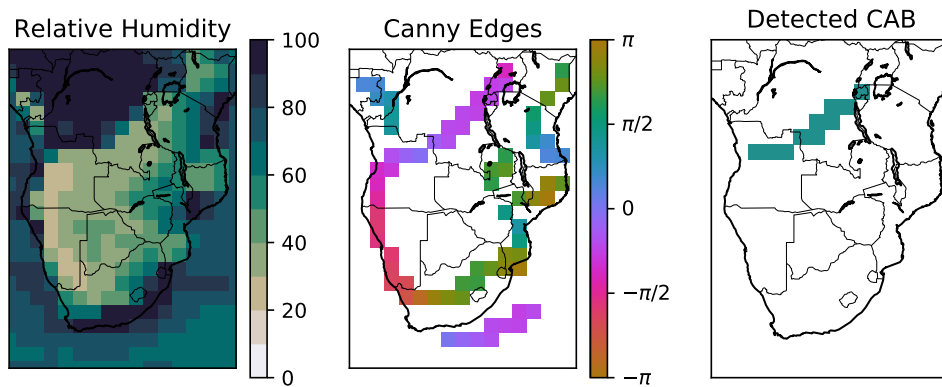
851 **Fig. 5.** Seasonal cycles of CAB properties. Top: mean CAB latitude, second row: CAB
852 frequency, and third row: CAB extent (number of grid cells identified per day).
853 Thin colored lines indicate models, and are ordered by the mean CAB latitude
854 averaged from August to November. Black lines show reanalysis products, thick
855 blue lines show the ensemble mean. All quantities are smoothed by a 2-week
856 running mean. 48

857 **Fig. 6.** Seasonal cycles of future change of CAB properties. As per Figure 5, but showing
858 the average of each property for the RCP8.5 end of 21st century scenario, minus
859 that for the historical end of 20th century scenario. The thick blue line indicates
860 the ensemble mean and is shown as a solid line when the ensemble mean is
861 significantly different from zero at the $p < 0.05$ level using a paired t-test, and
862 a dotted line otherwise. All quantities are smoothed by a 2-week running mean.
863 The bottom panel indicates the number of models for which the future change
864 signal is significant against internal variability at a $p < 0.05$ level for each month,
865 using a Welch’s t-test. Colors are ordered as per Figure 5. Colors in the top 3
866 panels are ordered as per Figure 5. 49

867 **Fig. 7.** CAB rainfall decomposition. Top row: historical rainfall, middle row: RCP8.5
868 minus historical. The bottom row compares the inter-model spread in historical
869 (blue) and RCP8.5 (red) simulations, and shows the number of models which
870 exhibit a significant change relative to interannual variability at the $p < 0.05$
871 level, based on a paired t-test (green line, top axis labels). First column: total
872 rain. Following columns show rainfall that falls: north of the CAB (second
873 column), south of the CAB (third column) and during CAB break down (last
874 column). All panel show October - December mean. Colors are ordered as per
875 Figure 5. 50

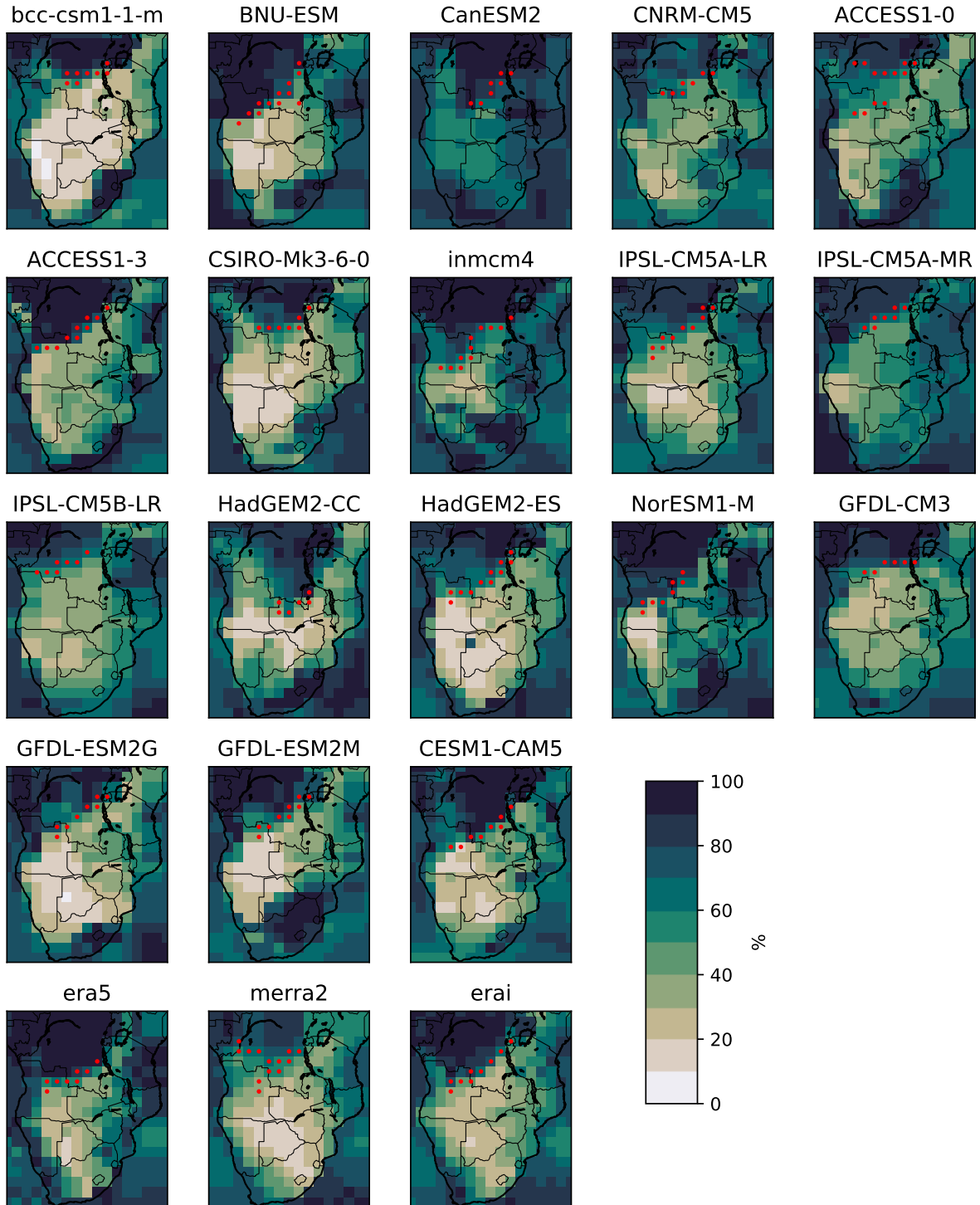
876 **Fig. 8.** Top row: Ensemble mean rainfall change OND based on CAB decomposition.
877 Bottom row: Linear regression between rainfall OND change in the region 15° -
878 30° E, 5° - 25° S and the November-December CAB frequency change. Black line:
879 least squares regression, text: p-value for the test that the slope of the regression
880 is equal to zero, and Pearson’s correlation coefficient. Left column: total rainfall,
881 centre column: rain that occurs north of the CAB, right column: rain that occurs
882 during CAB breakdown events. Colors are ordered as per Figure 5. 51

883	Fig. 9. Spatial distributions of tropical lows per $2 \times 2^\circ$ grid cell. Panels indicate different	
884	models, ensemble mean and reanalysis products.	52
885	Fig. 10. Normalized distributions (left and centre) and overall quantities (right) of trop-	
886	ical low properties. Top left: Longevity of TL events in days. Top centre:	
887	track latitude. Top right: total number of tropical low days per year for each	
888	model/reanalysis product. Bottom left: T63 filtered vorticity. Bottom centre:	
889	track zonal velocity, calculated as the tendency of the track longitude. Bottom	
890	right: proportion of rainfall attributable to tropical lows, based on the method-	
891	ology described in section 4b averaged over 15° - 30° E and 10° - 25° S. Thin colored	
892	lines indicate models, and are ordered by the maximum bin frequency of the up-	
893	per left panel. Black lines show reanalysis products, thick blue lines show the	
894	ensemble mean. Numbers in brackets indicate the number of models which show	
895	a significant change relative to natural variability at a $p < 0.05$ level based on a	
896	Mann Whitney U-test for the left column, and a Welch's t-test for the remaining	
897	panels.	53
898	Fig. 11. Proportion of rainfall attributed to tropical lows from December to February in	
899	historical CMIP5 sample. Rainfall is defined to be associated to a tropical low	
900	if it falls within 5° of the tropical low centroid. Panels show different CMIP5	
901	models and the ensemble mean.	54
902	Fig. 12. Changes in the distributions of tropical lows per grid-box per year between the	
903	RCP8.5 sample and the historical sample in each model and in the ensemble	
904	mean. Hatching on individual model panels indicates changes that are significant	
905	relative to interannual variability using a Welch's t-test. Forward (backward)	
906	hatching indicates significance at a $p < 0.1$ ($p < 0.05$) level. Ensemble mean:	
907	forward hatching indicates changes that are significant relative to the inter-model	
908	spread at a $p < 0.05$ level using a paired t-test.	55
909	Fig. 13. Filled contours: total rainfall change between RCP8.5 end of 21 st century sample	
910	and historical end of 20 th century sample for December to February over southern	
911	Africa. Purple: decrease, green: increase. Line contours: same as filled contours,	
912	but only for rainfall that has been attributed to tropical lows. Data that is	
913	insignificant at a $p < 0.05$ level relative to interannual variability (inter-model	
914	spread) based on a Welch's t-test (paired t-test) is masked for each model (for	
915	the ensemble mean).	56
916	Fig. 14. Upper row: spatial correlation between rainfall change components and tropical	
917	low spatial distribution change. Rainfall change and tropical low distribution	
918	change were calculated on a $2^\circ \times 2^\circ$ grid before correlation, and only mainland	
919	points between 5° - 25° S were considered. Lower row: inter-model regression be-	
920	tween overall rainfall change and tropical low frequency change, averaged over	
921	the same region as listed above. Left column: change in total rainfall field. Cen-	
922	tre column: change in rainfall located within 5 degrees of a tropical low. Right	
923	column: remainder rainfall.	57



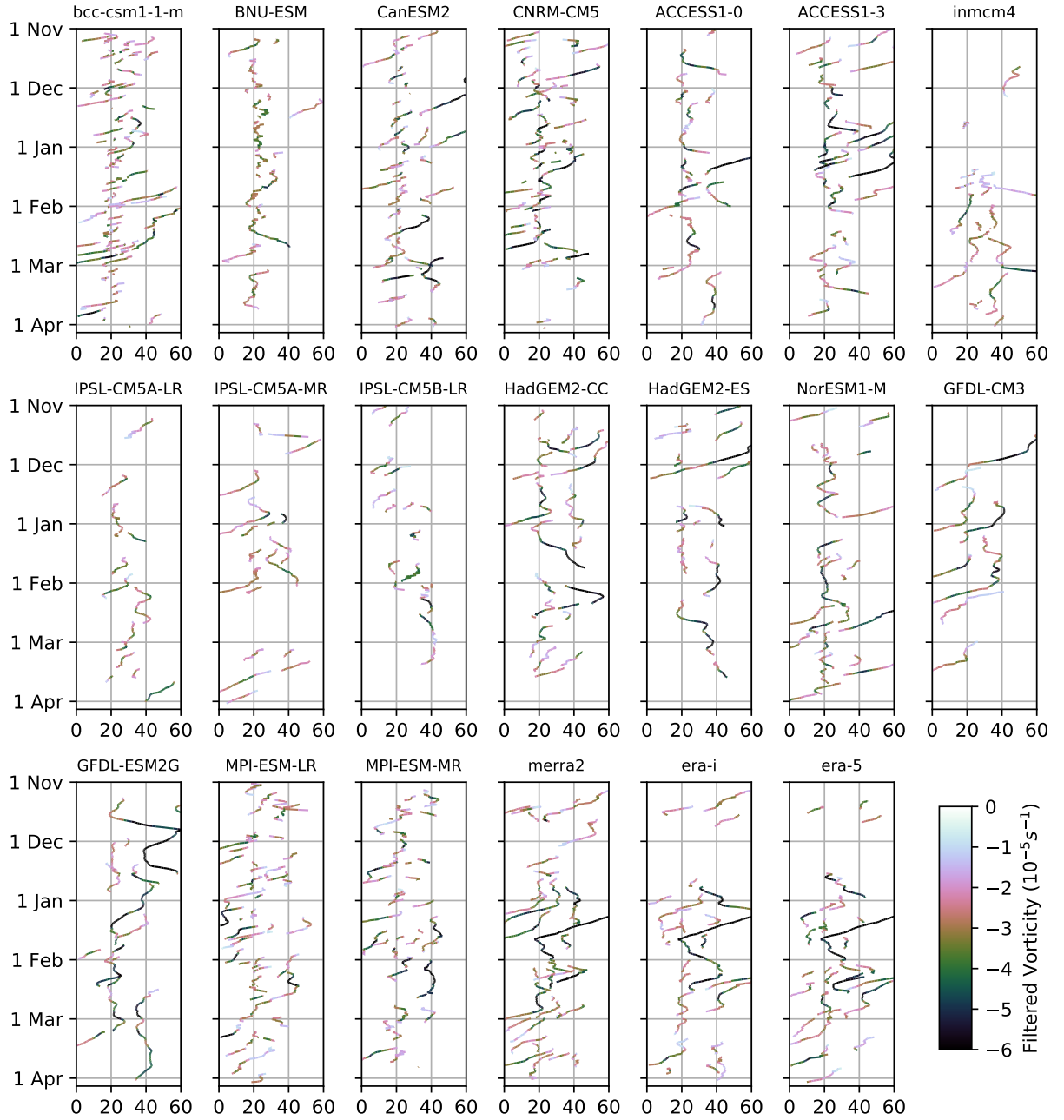
924 FIG. 1. Surface relative humidity (left panel), Canny edges (middle panel) and identified CAB
 925 locations (right panel) on the 9th of September 1999 in ACCESS1.3.

Surface Relative Humidity and Dry-lines on the 9th of September, 1999



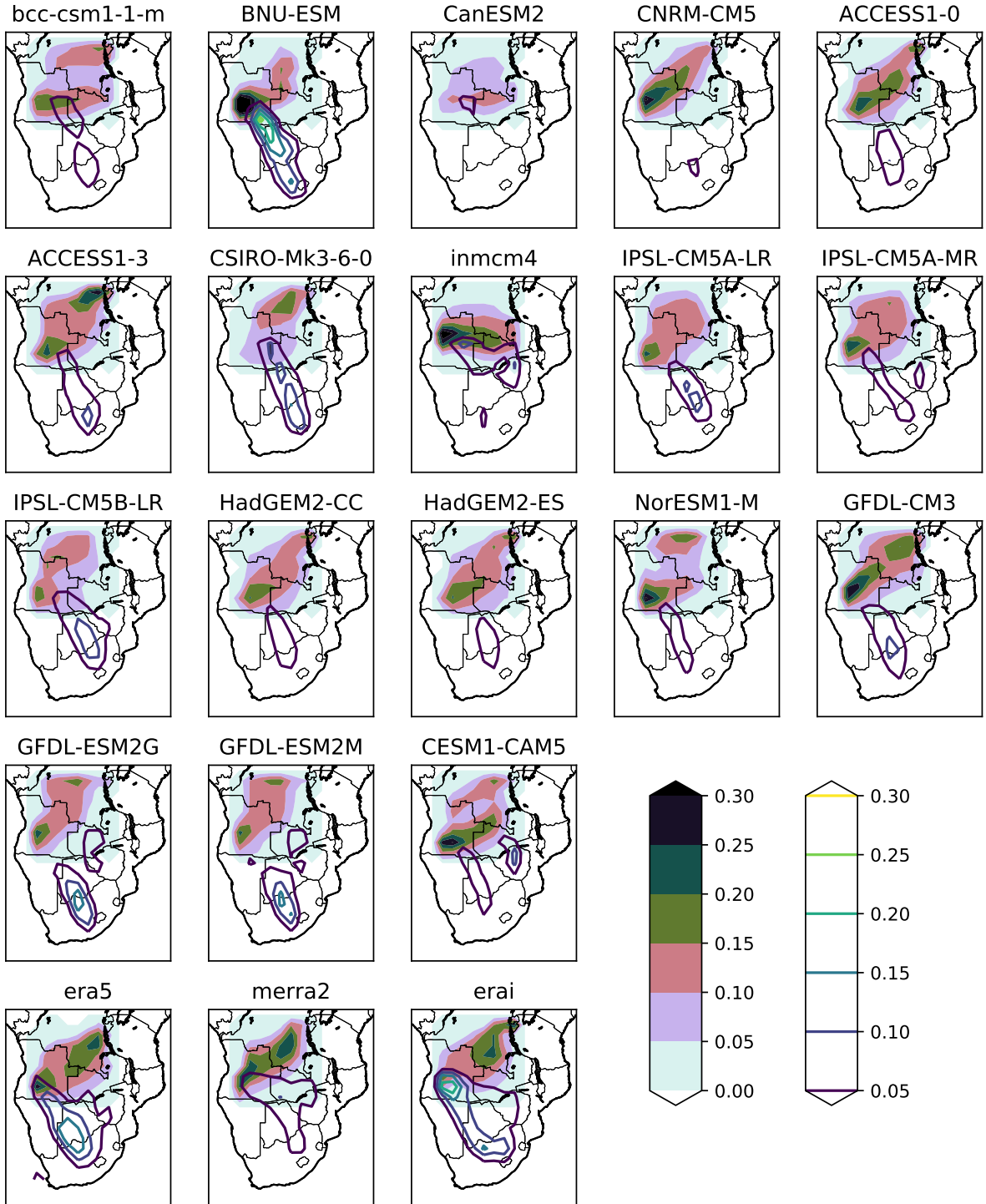
926 FIG. 2. Surface relative humidity (colors) and identified CAB locations (red dots) on the 9th of
 927 September 1999 in each model and reanalysis product. Surface humidity has been regridded to a
 928 $2^\circ \times 2^\circ$ grid using the nearest neighbor method.

Track Longitudes in 1986-1987

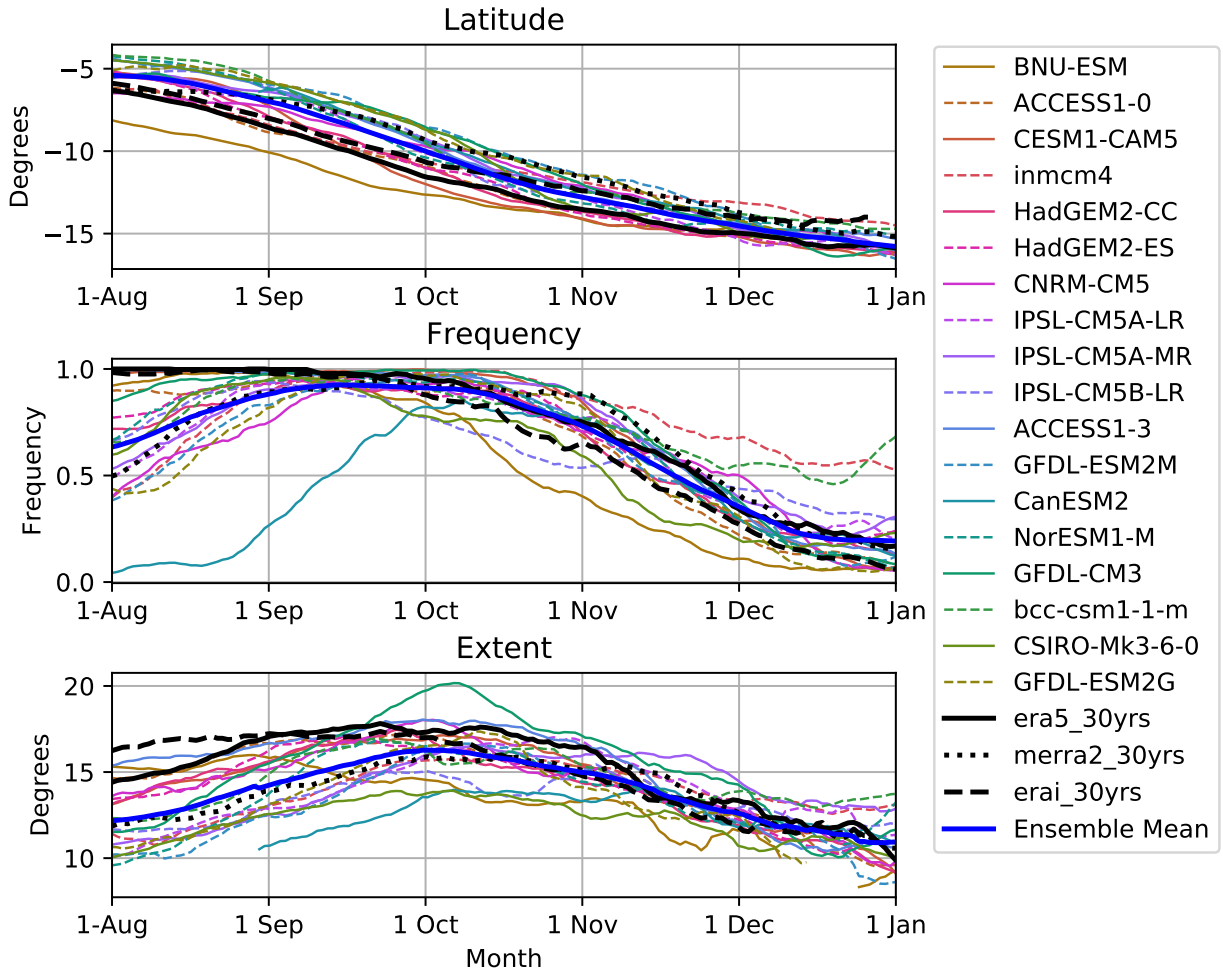


929 FIG. 3. Tropical low track Hovmöller plots for each model and reanalysis product. x -axis:
 930 longitude, y -axis: time. Colors indicate the T63 filtered vorticity of the tropical low event, a
 931 measure of the event intensity.

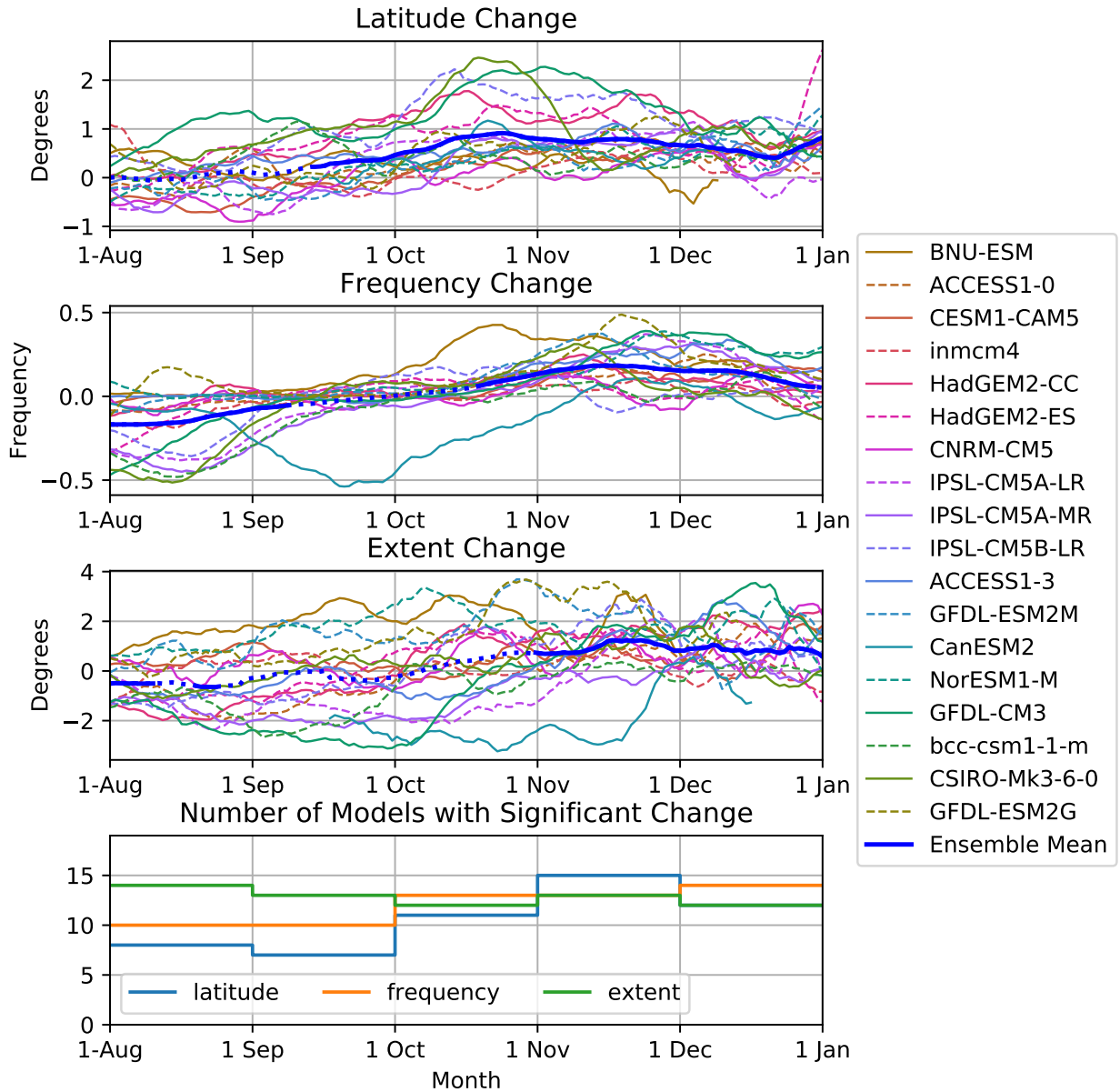
Proportion of days with CAB or KD identified at each grid point



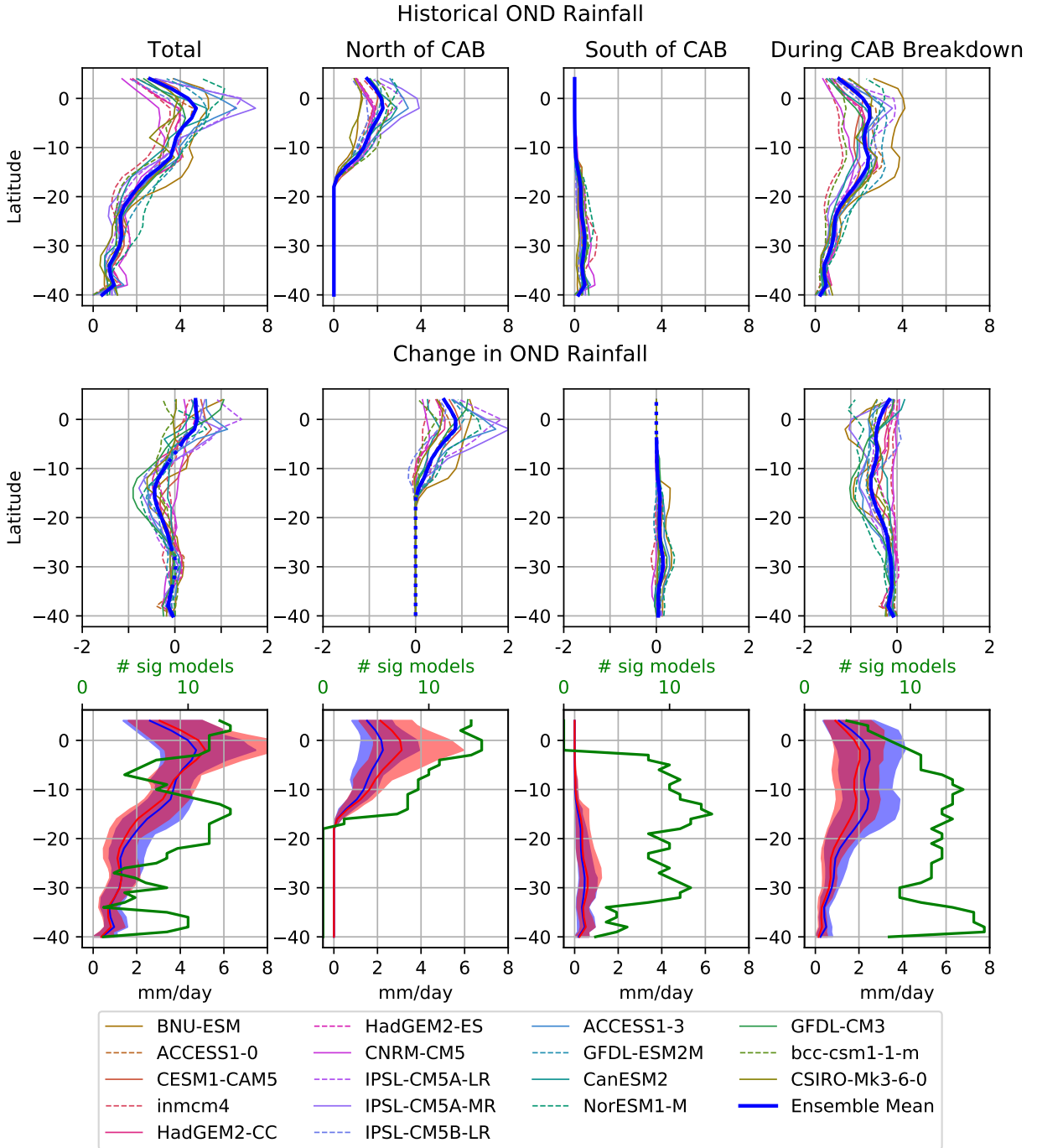
932 FIG. 4. Spatial distributions of CAB and KD frequency (number of events per interpolated grid
 933 cell per year). Filled contours: CAB. Line contours: KD. Panels indicate different models and
 934 reanalysis products.



935 FIG. 5. Seasonal cycles of CAB properties. Top: mean CAB latitude, second row: CAB fre-
 936 quency, and third row: CAB extent (number of grid cells identified per day). Thin colored lines
 937 indicate models, and are ordered by the mean CAB latitude averaged from August to November.
 938 Black lines show reanalysis products, thick blue lines show the ensemble mean. All quantities are
 939 smoothed by a 2-week running mean.

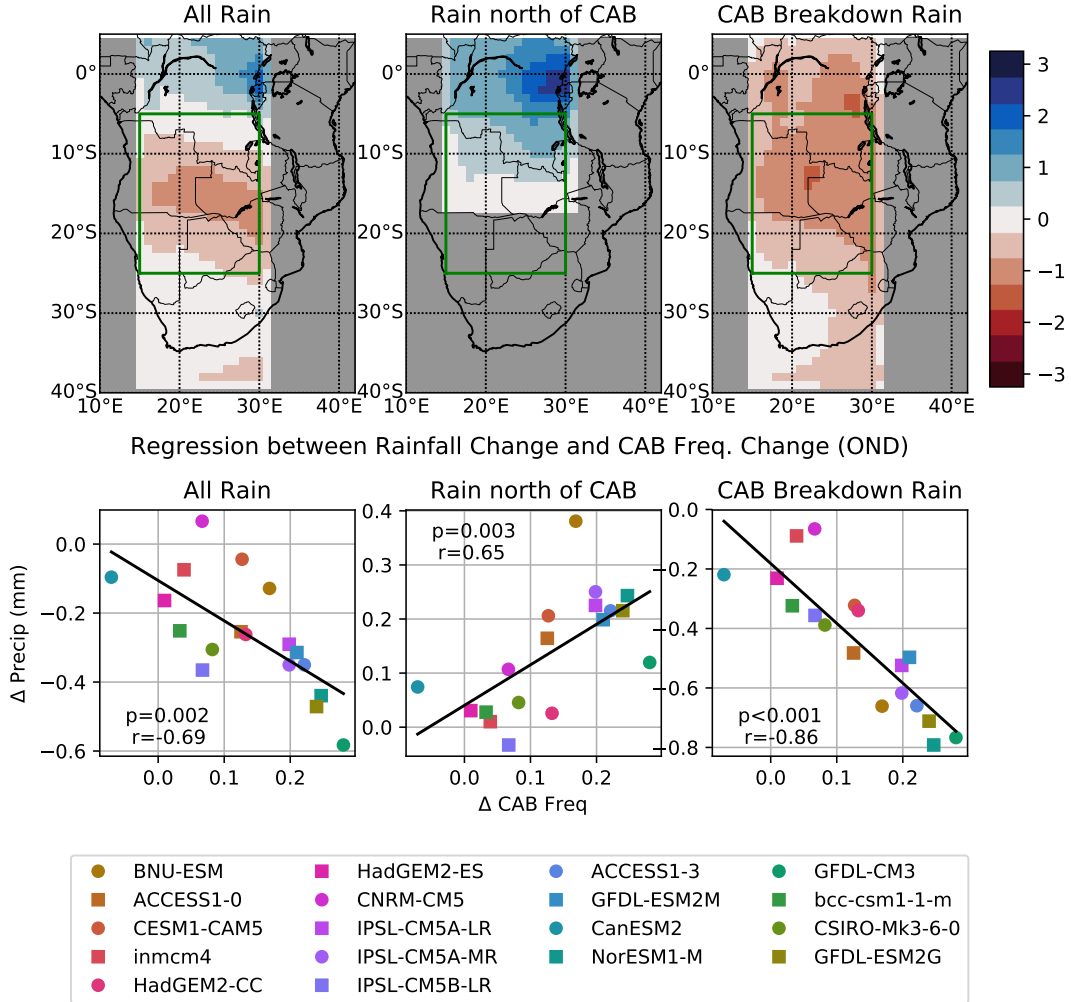


940 FIG. 6. Seasonal cycles of future change of CAB properties. As per Figure 5, but showing the
 941 average of each property for the RCP8.5 end of 21st century scenario, minus that for the historical
 942 end of 20th century scenario. The thick blue line indicates the ensemble mean and is shown as a
 943 solid line when the ensemble mean is significantly different from zero at the $p < 0.05$ level using a
 944 paired t-test, and a dotted line otherwise. All quantities are smoothed by a 2-week running mean.
 945 The bottom panel indicates the number of models for which the future change signal is significant
 946 against internal variability at a $p < 0.05$ level for each month, using a Welch's t-test. Colors are
 947 ordered as per Figure 5. Colors in the top 3 panels are ordered as per Figure 5.

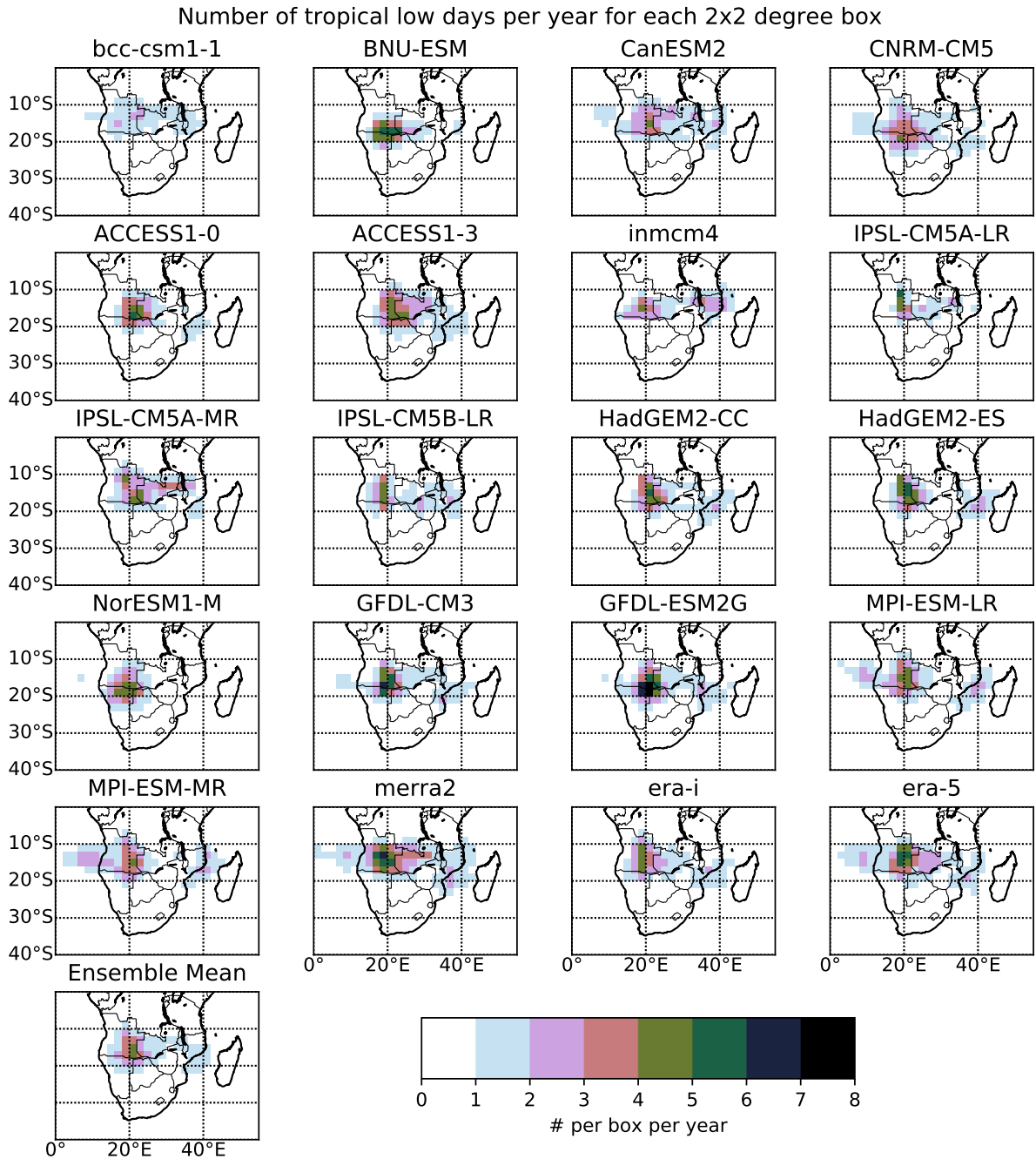


948 FIG. 7. CAB rainfall decomposition. Top row: historical rainfall, middle row: RCP8.5 minus
 949 historical. The bottom row compares the inter-model spread in historical (blue) and RCP8.5
 950 (red) simulations, and shows the number of models which exhibit a significant change relative to
 951 interannual variability at the $p < 0.05$ level, based on a paired t-test (green line, top axis labels).
 952 First column: total rain. Following columns show rainfall that falls: north of the CAB (second
 953 column), south of the CAB (third column) and during CAB break down (last column). All panel
 954 show October - December mean. Colors are ordered as per Figure 5.

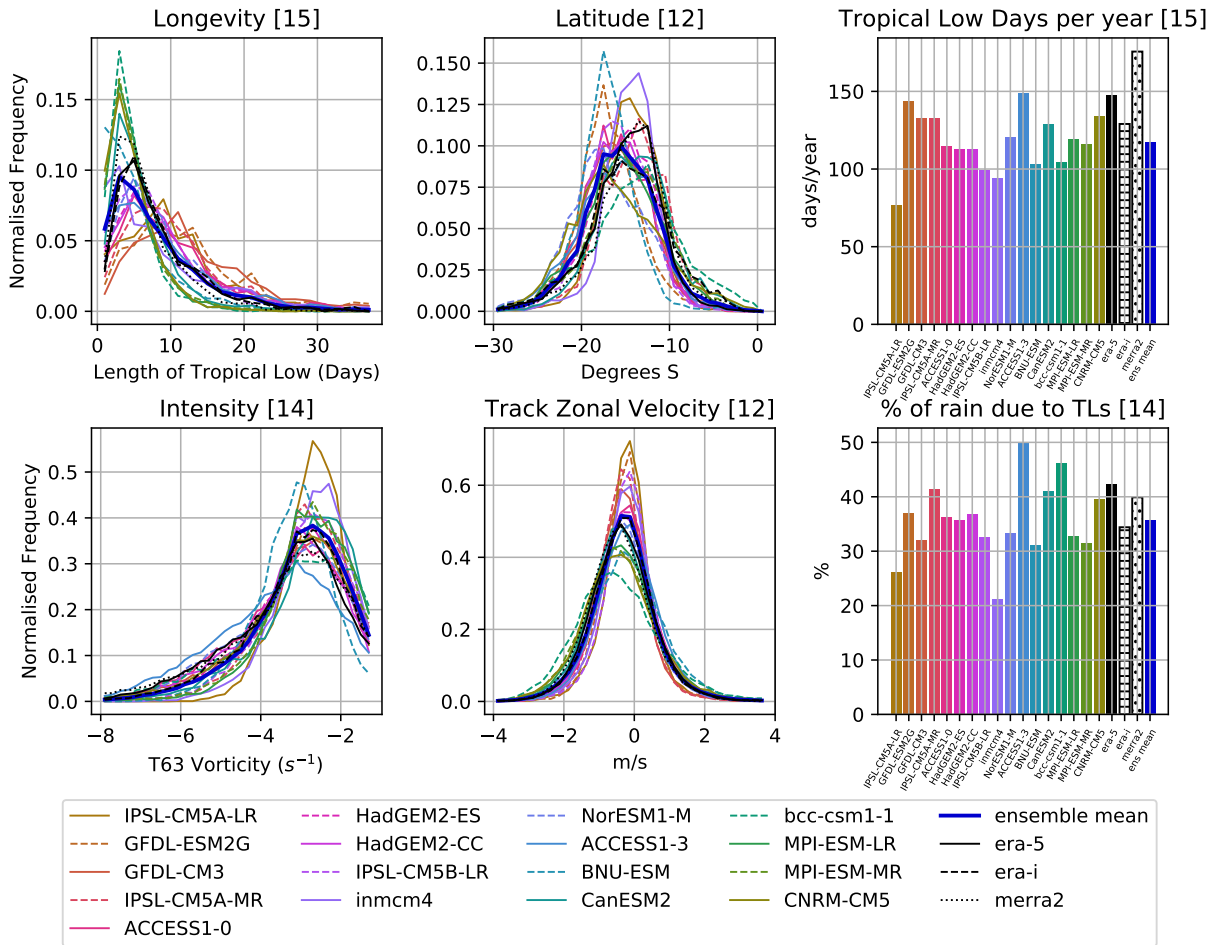
Ensemble mean rainfall change (OND)



955 FIG. 8. Top row: Ensemble mean rainfall change OND based on CAB decomposition. Bottom
 956 row: Linear regression between rainfall OND change in the region 15°-30 °E, 5°-25°S and the
 957 November-December CAB frequency change. Black line: least squares regression, text: p-value for
 958 the test that the slope of the regression is equal to zero, and Pearson's correlation coefficient. Left
 959 column: total rainfall, centre column: rain that occurs north of the CAB, right column: rain that
 960 occurs during CAB breakdown events. Colors are ordered as per Figure 5.

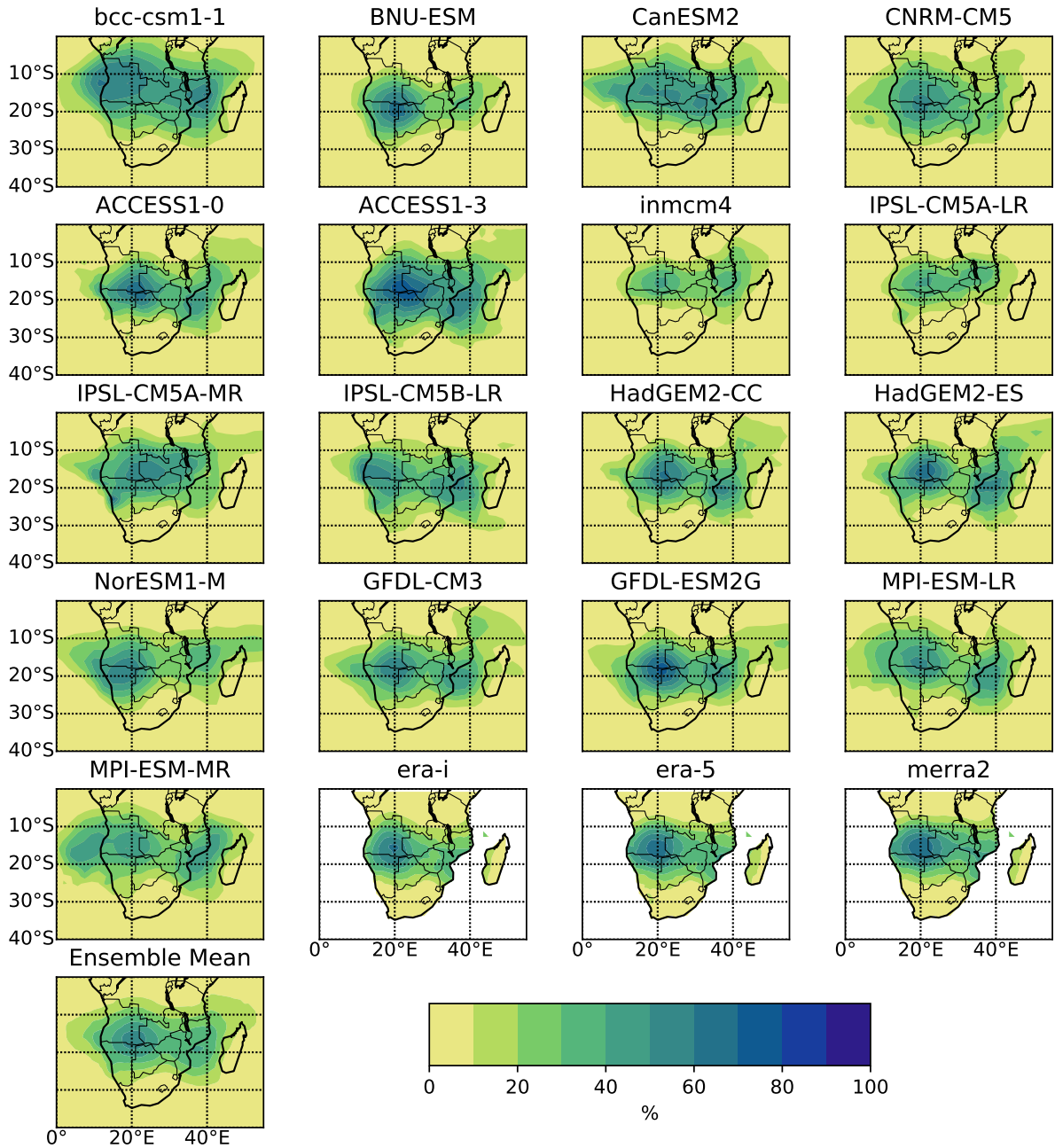


961 FIG. 9. Spatial distributions of tropical lows per $2 \times 2^\circ$ grid cell. Panels indicate different models,
 962 ensemble mean and reanalysis products.



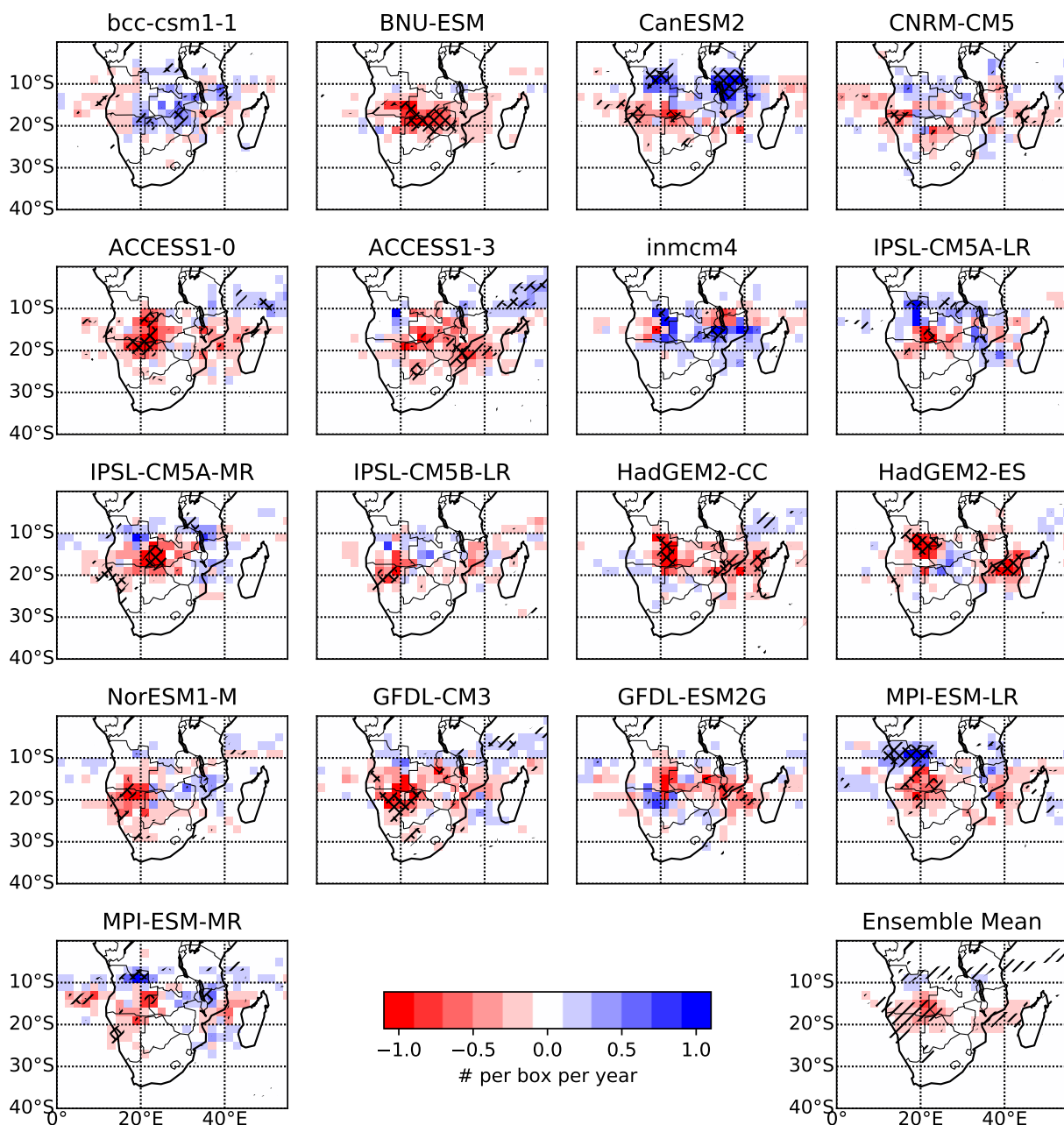
963 FIG. 10. Normalized distributions (left and centre) and overall quantities (right) of tropical
 964 low properties. Top left: Longevity of TL events in days. Top centre: track latitude. Top
 965 right: total number of tropical low days per year for each model/reanalysis product. Bottom
 966 left: T63 filtered vorticity. Bottom centre: track zonal velocity, calculated as the tendency of
 967 the track longitude. Bottom right: proportion of rainfall attributable to tropical lows, based on
 968 the methodology described in section 4b averaged over 15°-30°E and 10°-25°S. Thin colored lines
 969 indicate models, and are ordered by the maximum bin frequency of the upper left panel. Black
 970 lines show reanalysis products, thick blue lines show the ensemble mean. Numbers in brackets
 971 indicate the number of models which show a significant change relative to natural variability at a
 972 $p < 0.05$ level based on a Mann Whitney U-test for the left column, and a Welch's t-test for the
 973 remaining panels.

Proportion of CMIP5 DJF rainfall attributed to Tropical Lows



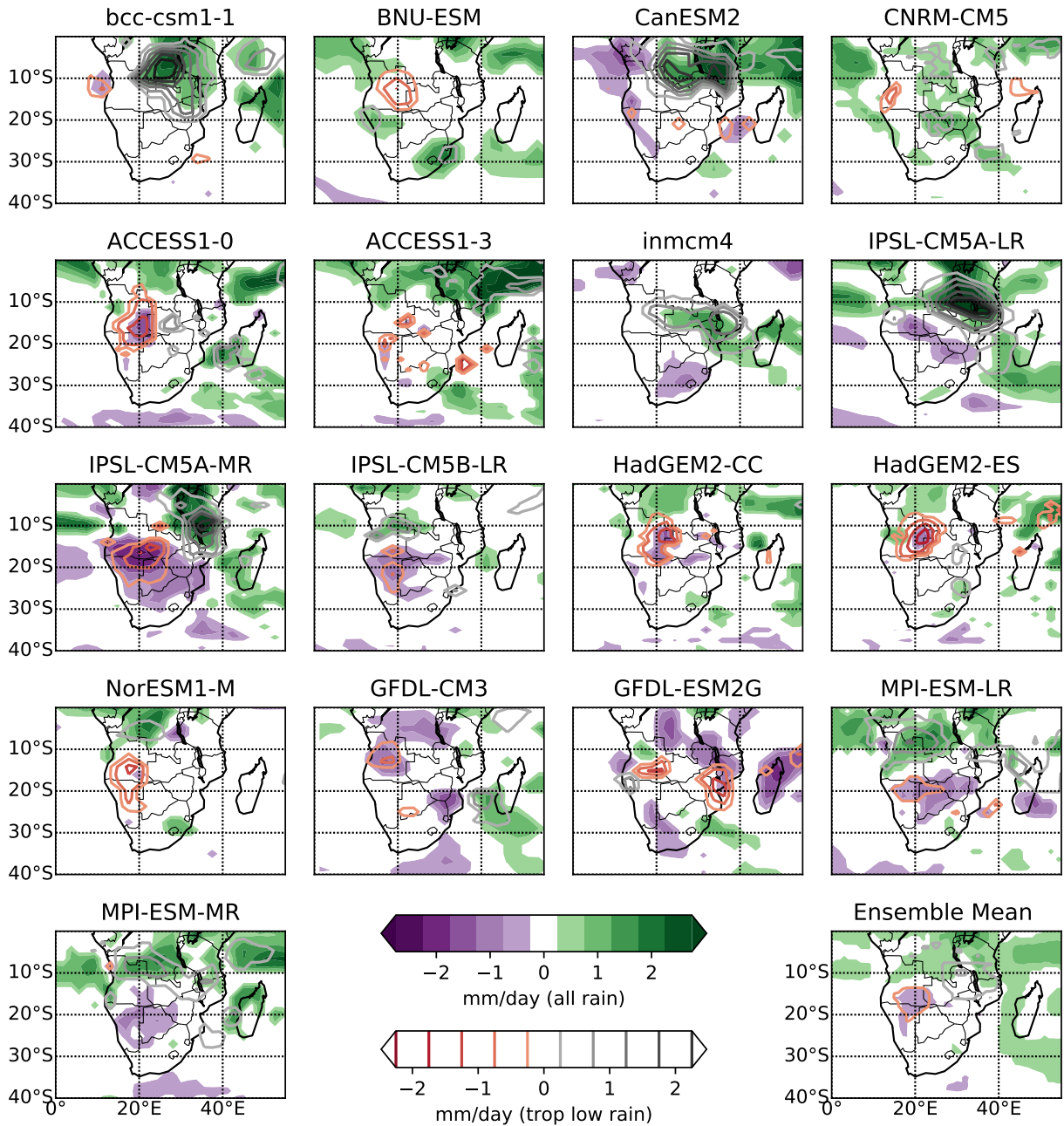
974 FIG. 11. Proportion of rainfall attributed to tropical lows from December to February in historical
 975 CMIP5 sample. Rainfall is defined to be associated to a tropical low if it falls within 5° of the
 976 tropical low centroid. Panels show different CMIP5 models and the ensemble mean.

RCP8.5 Change in the number of tropical lows per year located in each 2x2 degree box



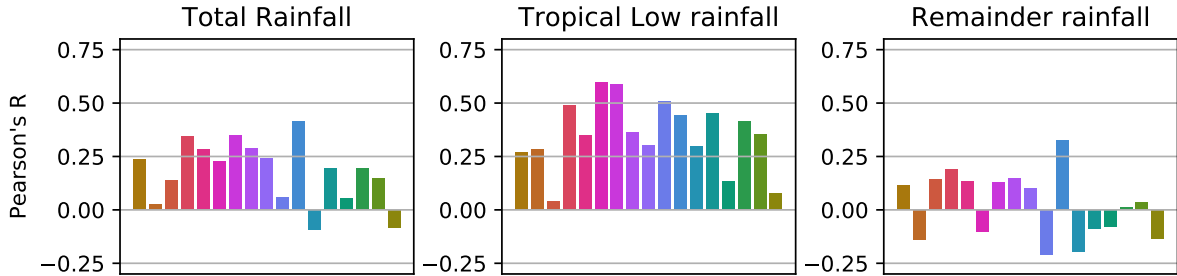
977 FIG. 12. Changes in the distributions of tropical lows per grid-box per year between the RCP8.5
 978 sample and the historical sample in each model and in the ensemble mean. Hatching on individual
 979 model panels indicates changes that are significant relative to interannual variability using a Welch's
 980 t-test. Forward (backward) hatching indicates significance at a $p < 0.1$ ($p < 0.05$) level. Ensemble
 981 mean: forward hatching indicates changes that are significant relative to the inter-model spread at
 982 a $p < 0.05$ level using a paired t-test.

CMIP5 DJF rainfall change: total (colours) and tropical low component (lines)

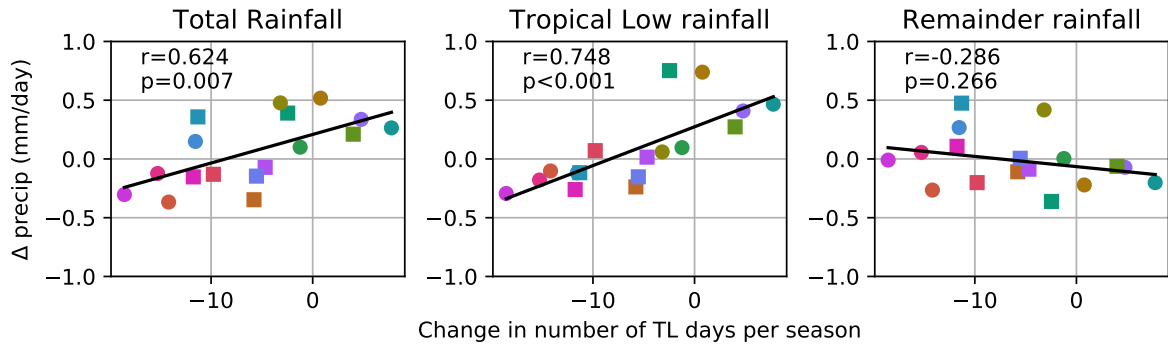


983 FIG. 13. Filled contours: total rainfall change between RCP8.5 end of 21st century sample and
 984 historical end of 20th century sample for December to February over southern Africa. Purple:
 985 decrease, green: increase. Line contours: same as filled contours, but only for rainfall that has
 986 been attributed to tropical lows. Data that is insignificant at a $p < 0.05$ level relative to interannual
 987 variability (inter-model spread) based on a Welch's t-test (paired t-test) is masked for each model
 988 (for the ensemble mean).

Spatial Correlation between TL change and Rainfall Change



Area Averaged Regression between TL change and Rainfall Change



989 FIG. 14. Upper row: spatial correlation between rainfall change components and tropical low
 990 spatial distribution change. Rainfall change and tropical low distribution change were calculated on
 991 a $2^\circ \times 2^\circ$ grid before correlation, and only mainland points between 5° - 25° S were considered. Lower
 992 row: inter-model regression between overall rainfall change and tropical low frequency change,
 993 averaged over the same region as listed above. Left column: change in total rainfall field. Centre
 994 column: change in rainfall located within 5 degrees of a tropical low. Right column: remainder
 995 rainfall.